

## **Reviewer 1**

The paper is interesting and presents a useful methodology for coastal flood modeling. The validation against a hydrodynamic model is OK but a bit questionable; this should be done against historical flood maps. A few assumptions should be also clarified. Limitations, uncertainties and implications need to be further discussed. I have recommended several edits and some comments in the PDF. Here are some additional comments:

**Response:** Thank you for the detailed review and the constructive comments.

Please provide more information on the study catchment, particularly those that affect your model results. This includes computational area, soil type, channels' size, ground slope, land use etc.

**Response:** We have included additional information in the revised manuscript regarding the study catchment (**Section 2; Lines 148-159**) and model domain (**Section 3.1.1; Line 237**). In short, the average slope, length, and annual discharge of the Savannah River are 0.00011 m/m, 505 km, and 320 m<sup>3</sup>/s, respectively. Also, the river bathymetry was deepened up to 12 m for increasing the capacity of cargo transportation according to the U.S. Army Corps of Engineers. The model domain comprises an area of 1178 km<sup>2</sup> approximately.

Section 2: Present the source of drainage network data. Also, how detailed does that represent the drainage network?

**Response:** Drainage network data including river streams, tidal channels, and creeks within wetland areas can be obtained from the U.S. National Wetlands Inventory (<https://www.fws.gov/wetlands/data/Mapper.html>). These publicly available data are continuously updated by the U.S. Fish and Wildlife Service (FWS) and are derived from multiple data sources including satellite imagery and aerial photos of 1 m (or less) digital color infrared imagery. We included this information in Section 2 (**Lines 157-159**).

The verification of the approach against flood maps generated by a hydrodynamic model is questionable. How well is the model calibrated? For what historical events (how large/intense), it has been calibrated? Also, why not using satellite imagery like Dartmouth Flood Observatory?

**Response:** The primary goal of this manuscript is to propose a low complexity flood mapping (LCFM) method whose accuracy is comparable with a computationally expensive hydrodynamic model. Therefore, we compare our results with a hydrodynamic model to assess if our method can be a proper replacement of these models. This is the idea of proposing surrogate models that mimic the performance of complex physically-based models. A similar approach has been presented recently where surrogate machine learning methods are trained and validated against a well-calibrated hydrodynamic model. The hydrodynamic model has been calibrated for both non-extreme events and two major Hurricanes in the region, namely Hurricanes Matthew and Irma. Please see details of the calibration in **Figure 4** and **lines 382-398** in the revised manuscript.

Using satellite imagery has major limitations. 1) These maps are rarely available for the peak date of a flood event while we are looking for the maximum flood hazard maps. 2) These

maps only provide the extent of flooding (HDC=0) while we need floodwater depths to generate flood hazard maps for different levels of HDCs. For example, here we validate for both HDC=0 and HDC=0.6 m. 3. Daily satellite data, such as Dartmouth Flood Observatory uses coarse-scale satellite imagery, such as MODIS with 250-500 m spatial resolution that is not appropriate for validation. We need a much finer scale (<30 m) for validating our maps.

Please discuss the properties of the high-performance computing system that was used for simulations (Section 3.1.2).

**Response:** We used available computational resources of the University of Alabama (UA) for running model simulations in parallel. The UAHPC is a 87 node (1660 core) cluster featuring Dell PowerEdge M610s, M620s, and M630s. The nodes contain two Intel 8-Core E5-2650, E5-2640v2, or 10-core E5-2640v3 processors and at least 64GB of RAM per node. More information of UAHPC can be accessed in the following link: <https://oit.ua.edu/services/research/>. Nevertheless, we consider this information only relevant for the reviewer.

More details on the LHS application are needed. How was it informed by Hurricane Matthew peak WLs? What parameters were considered as uncertain? What probability distributions were used and how were they characterized?

**Response:** The Latin Hypercube Sampling (LHS) technique was used to sample 200 sets of roughness ( $n$ ) values for model calibration. We considered a 7-day window around peak water levels (e.g., peak surge of Hurricane Matthew) to evaluate the model's performance. In that way, we identify the optimal combination of  $n$ -values (among the 200 model simulations) that accurately represent both non-extreme (low water) and extreme WLs. For simplicity, we only considered  $n$ -values as uncertain parameters and assumed that any errors follow a Gaussian distribution as discussed in Helton and Davis (2003). The advantage of LHS over traditional Monte Carlo approaches is that the former results in a denser stratification over the range of each sampled parameter as compared to random sampling. Hence, LHS leads to more stable results that are closer to the true probability density function (PDF) of the parameter. We included this information in **Section 3.1.2 (Lines 251-254)**.

Please discuss how the performance of model was graded based on the fit metrics (RMSE, AUC and  $R^2$ ). You may refer to Moriasi et al. (2015) and Ahmadisharaf et al. (2019) for streamflow predictions via  $R^2$  or others for flood simulations. Neither RMSE nor  $R^2$  measure bias. Metrics like PBIAS need to be used along to measure the model performance.

**Response:** We have included additional metrics to evaluate model's performance more rigorously: Kling-Gupta Efficiency (KGE), and Nash-Sutcliffe Efficiency (NSE). In addition, we have replaced  $R^2$  by mean absolute bias (MAB). NSE measures the relative magnitude of the error variance of model simulations compared to the variance of observational data (Nash and Sutcliffe, 1970). NSE ranges between  $-\infty$  to 1, where an efficiency of 1 indicates a perfect match between simulated and observed WLs. Kling-Gupta efficiency (KGE) is a robust evaluation metric that accounts for correlation, bias, and ratio of variances (Gupta et al., 2009). KGE can take values between  $-\infty$  and 1, where an efficiency of 1 indicates a perfect match. Mean absolute bias (MAB) quantifies the bias of model simulations with respect to

observational data. MAB of 0 suggests an absence of bias in the simulations. This information and further discussion of model results are included in [Section 3.1.2 \(Lines 260-268\)](#) and [Section 4 \(Lines 358-360\)](#), respectively.

Please define what 'error' exactly is in the model evaluations under the Results section.

**Response:** Error is the summation of rate of false positives and rate of false negatives in binary classification problems. We have defined this metric in [Equation 5 and lines 349-353](#) in the revised manuscript as follows:

“In binary classification, positive and negative refer to a value of one and zero, respectively. True positive instances are those positive cells that are correctly predicted by the classifier and false positive instances represent those negative cells that are wrongly classified as positive. The *error*, reflecting all cells that are wrongly predicted by the classifier, is a commonly-used measure for validating the performance of binary classifiers for flood hazard mapping. “

Please discuss what probability distributions exist in the MATLAB allfitdist tool.

**Response:** 'allfitdist' tool includes the following parametric probability distributions:

Continuous: Beta, Birnbaum-Saunders, Exponential, Extreme value, Gamma, Generalized extreme value, Generalized Pareto, Inverse Gaussian, Logistic, Log-logistic, Lognormal, Nakagami, Normal, Rayleigh, Rician, t location-scale, and Weibull.

Discrete: Binomial, Negative binomial, and Poisson. We believe this information is not relevant for the main goal of this study.

The underlying assumption of a univariate flood frequency analysis is that a peak WL with a given return period leads to a flood event with the same return period. However, studies (e.g., Brunner et al. 2016) have shown that a combination of peak flow and other attributes like volume may lead to a different return period. This limitation should be at least acknowledged in the paper.

**Response:** Thank you for the great suggestion. We discussed this limitation and added an appropriate reference. Please refer to [lines 560-564](#) in the revised manuscript.

Further details are needed on how TH and HDC are derived. As of now, it appears that they are subjectively derived.

**Response:** TH is the threshold of the hydrogeomorphic classifier that should be calibrated by optimizing the error measure calculated from the comparison of reference and simulated maps. Therefore, this variable is derived from optimization results and is not derived from subjective decisions. HDC, however, is the hazard depth cutoff that converts the continuous flood depth map to a binary flood hazard map. This is a control variable that the decision maker (emergency responder) should pick from. We use 21 HDC resulting from 0.1 increments in the range of 0-2 m and show the results (TH) for all these HDCs. This provides 21 points for generating a smooth curve (Figure 7) so that the decision-maker can

simply use this curve and pick the required TH according to different values of HDCs. Please refer to [lines 356-378](#) in the revised manuscript.

MAB has been reported in the Results section but not in the Methods section. Please either remove it from the Results section or discuss it in the Methods section.

**Response:** We have included a description of MAB in the revised manuscript ([Section 3.1.2, Lines 260-268](#)).

There should be a plot on calibrating  $w_1$  and  $w_2$  coefficients (for the  $H$  and  $D$  variables).

**Response:** Yes, we already included this plot in the manuscript. Please see [Figure 6b](#) where we show how calibrated  $w_1$  and  $w_2$  values change for different HDCs. The higher weight of  $w_1$  compared to  $w_2$  shows that feature  $H$  is more important than feature  $D$ .

L429-432: Reasons for this poor performance need to be discussed in the Discussion Section.

**Response:** We added more text that explains the potential reasons for the discrepancies between the hydrogeomorphic method and hydrodynamic model results. Please refer to [lines 481-488](#) in the revised manuscript as follows:

“The main discrepancies are some noisy scattered low-hazard areas located in the east and southeast of the study area. These areas can reflect the flooded surface depressions (sinks) resulting from the pluvial impacts of extreme precipitation. Hydrodynamic models simulate the fluvial and coastal processes that occur adjacent to rivers and oceans while disregarding the pluvial impacts. The red circle in the left part of the figures shows a region that the hydrogeomorphic method cannot properly simulate, especially for higher HDCs. This can be due to the inability of the hydrogeomorphic method to properly simulate physical processes.”

The comparison of computational time against the hydrodynamic model is unclear to me. Did you compare your static model against an unsteady Delft3D-FM or the steady-state? The runtime of an unsteady hydrodynamic model should not be very long; therefore, this advantage of your presented model is not as strong as it is presented.

**Response:** The Delft3d-FM simulates the flood in an unsteady condition. Due to the high nonlinearity and complexity of extreme floods, flood modeling in a steady state is highly erroneous. The runtime of a hydrodynamic model depends on the scale of the study area, and the number of grid cells. For a fine scale simulation (<10 m) performed for medium-large scale problems (> 1000 km<sup>2</sup>), the computational time of hydrodynamic models can take a few days. The main goal of using LCFM methods is to reduce the computational time while providing acceptable accuracy (improve the efficiency of modeling). For emergency responders, timing is the most important factor, thus having access to more efficient models that estimate the hazardous areas in order of minutes is significantly beneficial.

Broader impacts need to be discussed. The authors should discuss what implications these results have for coastal planners and floodplain managers etc. and what existing programs in the US (e.g., FEMA FIRMs) may benefit from this research.

**Response:** The Discussion section already touches on this topic a bit. We have expanded this discussion on the implications for coastal planners, floodplain managers, and existing U.S. programs (e.g., the NWS) in the Discussion section. (Lines 580-609)

“Operationally, the Sea, Lake, and Overland Surges from Hurricanes (SLOSH) model (Jelesnianski et al., 1984) is the storm surge model currently used by NWS to perform storm surge forecasting and create probabilistic flood inundation maps for real-time tropical storms (Sea, Lake, and Overland Surges from Hurricanes (SLOSH), 2022). The feature of SLOSH that makes it the preferred model of the NWS for storm surge forecasting and mapping is the model’s computational efficiency that allows the model to be run as an ensemble (Forbes et al., 2014). However, SLOSH is just one of several modeling options for storm surge modeling and mapping, each possessing strengths and weaknesses associated with their simulations. The inclusion of additional models that can create flood maps of storm surge for a given event should provide an enhanced understanding of the uncertainty of inundation at a given location (Teng et al., 2015). However, the higher computational burden of alternative models, such as Delft3D-FM, tend to preclude their use in real-time operations and certainly, their use in generating an ensemble necessary for probabilistic flood maps. The methodology we propose in this manuscript may offer the NWS and other agencies a means to utilize alternatives to SLOSH for flood inundation mapping and probabilistic flood inundation mapping on U.S. coastlines. Models such as Delft3D-FM can generate reference maps to train the binary classifier and build the probabilistic operating curves. The probabilistic operative curves would account for the major source of uncertainties and provide a computationally efficient and reliable decision-making tool for coastal planners and floodplain managers. The operative hydrogeomorphic threshold classifiers proposed for real-time coastal flood hazard mapping can be used as an alternative tool for the rapid estimation of hazardous areas during real-time flood events. In an operational mode, water level or meteorological forecasts can be used to estimate the return period of an upcoming coastal flood event and the methodology here can utilize this as an input to perform LCFM flood inundation mapping both deterministically and probabilistically.”

Study limitations and potential areas for future research need to be expanded.

**Response:** We have already included three areas of research for future studies. To expand this, we added more text explaining the study limitations and potential areas for future research. Please refer to lines 520-528 in the revised manuscript.

“The proposed hydrogeomorphic index ( $I_{HD}$ ) is the primary data for flood hazard mapping in this study. Thus, the quality of two main inputs of this index, namely the DEM and stream network used to calculate features H and D play a vital role in the overall accuracy of the proposed approach. To obtain maximum accuracy, here we used the best available DEM with the finest spatial resolution of 3 m that includes the bathymetry data. However, considering the limited access to such high-quality DEMs in many areas of the world, it is recommended to evaluate the sensitivity of the proposed approach to lower quality DEMs (e.g. 30 m and 90

m DEMs without bathymetry information) in future studies. Another piece of research can investigate the sensitivity of the proposed approach to the density of the drainage network used for calculating the  $I_{HD}$  index.”

In general here are the areas of research we recommended for future studies:

1. Sensitivity of the hydrogeomorphic index to DEM quality and stream network density (Lines 520-528)
2. Applying the proposed hydrogeomorphic operative curves to inland floods and to other deltas across the US. (Lines 544-550)
3. Improve the flood frequency analysis, considering its uncertainties, incorporating other sources of uncertainties in the modeling to generate probabilistic operative curves (Lines 556-577)
4. A benchmark study that compares the performance of three LCFM methods (Lines 617-620)

Sources of uncertainty and how they may affect your findings need to be discussed.

**Response:** This has been thoroughly addressed in the discussion section. Please refer to lines 556-579 in the revised manuscript.

“The reference maps used for training the binary classifier are key components for generating reliable results. Since these reference maps are the outcomes of hydrodynamic modeling, they are prone to uncertainties stemming from unrealistic parametrization, imperfect model structure, and erroneous forcing. The design floods used as boundary conditions of the hydrodynamic model are estimated from flood frequency analysis that is prone to uncertainty as well. Here we used a bivariate approach that estimates the design flood based on the water level data. A more comprehensive flood frequency analysis that accounts for other flood attributes, such as volume can improve the reliability of flood frequency analysis in future studies (Brunner et al., 2016). With access to less than 100 years of data for flood frequency analysis, the extreme return levels (i.e. 500- and 1000-year floods) pose high uncertainties due to the extrapolation of annual maxima data. This should warn decision-makers to be more cautious about using operative curves for extreme flood events. For future studies, the uncertainty bounds of flood frequency analysis (especially extrapolations for extreme cases) can be considered in the modeling. In a real-time scenario, the forecasted WL used for flood frequency analysis is also prone to uncertainties originating from imperfect forecasting methods and nonstationary climate data. In addition, the uncertainty of model parametrization can be accounted for by running the hydrodynamic model for different combinations of optimum parameters. Model structure uncertainty can be also considered by using different hydrodynamic models and combining the results. Finally, probabilistic reference maps together with uncertainties involved in WL forecasting and flood frequency analysis can be integrated to develop probabilistic hydrogeomorphic threshold operative curves in future studies. This is in line with the report provided for the NOAA National Weather Service (NWS), showing the NWS stakeholder’s preference for utilizing probabilistic storm surge inundation maps (Eastern Research Group, Inc, 2013).”

Please discuss how your presented modeling framework can be used in other study areas. What considerations should be taken to do so? Guidelines should be provided in the Discussion section.

**Response:** We added the following texts to address this concern of the reviewer. Please refer to **lines 550-555** in the revised manuscript.

“To implement this approach, first, a hydrodynamic model should be set up for the new study area and generate reference inundation maps for different return periods. Access to observed water level data (gauges or HWMs) and flood extent maps from past floods is required to properly calibrate the hydrodynamic model. Then the  $I_{HD}$  index calculated from a DEM is utilized together with the reference maps to provide the hydrogeomorphic threshold operative curves for future floods.”

Please spell out all the abbreviations in the headings, figures and tables. These need to stand alone.

**Response:** Done.

Please italicize all variables/parameters in the text.

**Response:** Done.

## **Reviewer 2**

The authors present an interesting work on flood hazard assessment and mapping. The paper is well-written and easy to follow. However, some issues need to be addressed before the paper can be accepted for publication as follows:

**Response:** Thank you for your positive feedback and the constructive comments on our manuscript. Please see our detailed response to the comments below:

The abstract should briefly state the purpose of the research, the principal results, and major conclusions. The abstract should be more descriptive rather than informative. More than half of this abstract is allocated to the research gaps which in my opinion is not appropriate (L24-36). Please revise the abstract section with more focus on your methods, and significant results/conclusions.

**Response:** Thanks for the suggestion on editing the abstract. We removed several lines from the first part of the abstract and added more texts to better describe the method and results of the proposed approach. Please see the revised abstract below:

“In the last decade, DEM-based classifiers based on Height Above Nearest Drainage (HAND) have been widely used for rapid flood hazard assessment demonstrating satisfactory performance for inland floods. The main limitation is the high sensitivity of HAND to the topography which degrades the accuracy of these methods in flat coastal regions. In addition, these methods are mostly used for a given return period and generate static hazard maps for past flood events. To cope with these two limitations, here we modify HAND, propose a composite hydrogeomorphic index and develop hydrogeomorphic threshold operative curves for rapid real-time flood hazard assessment in coastal areas. We select the Savannah river delta as a testbed, calibrate the proposed hydrogeomorphic index on Hurricane Matthew and validate the performance of the developed operative curves for Hurricane Irma. The hydrogeomorphic index is proposed as the multiplication of two normalized geomorphic features, HAND and distance to the nearest drainage. The calibration procedure test different combinations of the weights of these two features and determine the most appropriate index for flood hazard mapping. Reference maps generated by a well-calibrated hydrodynamic model, Delft3D-FM model, are developed for different water level return periods. For each specific return period, a threshold of the proposed hydrogeomorphic index that provide the maximum fit with the relevant reference map is determined. The collection of hydrogeomorphic thresholds developed for different return periods are used to generate the operative curves. Validation results demonstrate that the total cells misclassified by the proposed hydrogeomorphic threshold operative curves (summation of overprediction and underprediction) are less than 20% of the total area. The satisfactory accuracy of the validation results indicates the high efficiency of our proposed methodology for fast and reliable estimation of hazard areas for an upcoming coastal flood event which can be beneficial for emergency responders and flood risk managers.”

L167. Add one or two sentences to explain about Savannah model in Delft3D-FM.

**Response:** We have included more details of the Delft3D-FM suite package (Line 186-189). For additional details of the Savannah model, the reviewer is referred to section 3.1.

“Specifically, we used the 2021 Delft3D-FM suite package to model the complex interactions between riverine, estuarine, and intertidal flat hydrodynamics. The suite package can provide detailed information of water level, flow rates, and velocity (Delft3D Flexible Mesh Suite - Deltares, 2021)”

Using a univariate flood frequency analysis in an estuary region should be justified with a detailed analysis that shows there is no correlation between high river flow and sea water level. Otherwise, a bivariate flood frequency analysis should be considered.

**Response:** In the first steps of this study, we had set up the calibrated Delt3D-FM model for different combinations of upstream flow and downstream water levels. However, we did not find a significant correlation ( $p$ -value < 0.05) between river discharge at Clyo station (USGS - 02198500) and coastal water levels at Fort Pulaski station (NOAA - 8670870). The latter was also reported in Ghanbari et al., 2021 and Muñoz et al., 2020. Furthermore, our results demonstrated that high river flow does not affect the inundation area in wetland areas. This indicates that flood inundation is highly dominated by coastal forcing as tides propagate into the Savannah river and lead to flow reversal at upstream gauge stations (see Figure 1 below). The high proximity of wetlands to the Atlantic Ocean shows that the transitional zone, i.e., the area affected by both coastal and inland drivers, is located upstream Port Wentworth station (USGS - 02198920) where the Savannah river trifurcates into the Back River, Middle River, and Front River. Considering the dominant role of sea water level in coastal flooding as well as the negligible effect of river discharge on wetland inundation from the previous analyses, we can justify the proposed univariate flood frequency analysis. For the reviewer’s convenience we also generate a figure of maximum floodwater depth in Savannah under high river flow regimes (10 and 1000-year return period) and mean sea level (Figure 2). The flood maps indicate similar inundation patterns over coastal wetlands and clear differences in upstream zones. . Please refer to **Section 3.2 (Lines 277-288)** in the revised manuscript for additional justification of the univariate approach.

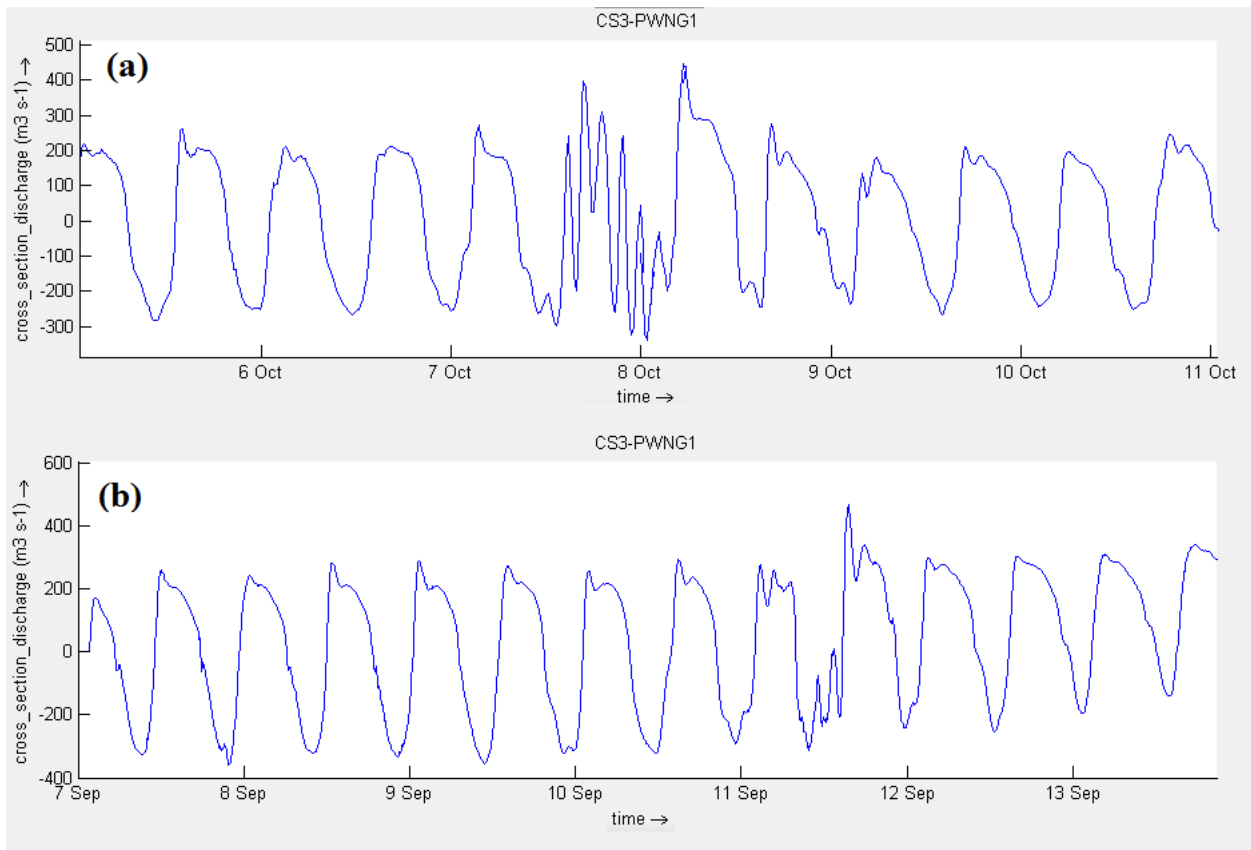


Figure 1. Flow reversal (negative river flow) due to tidal propagation at Port Wentworth station (USGS – 02198920). Simulations of averaged cross section discharge correspond to (a) Hurricane Matthew (Oct/2016) and (b) Hurricane Irma (Sep/2017).

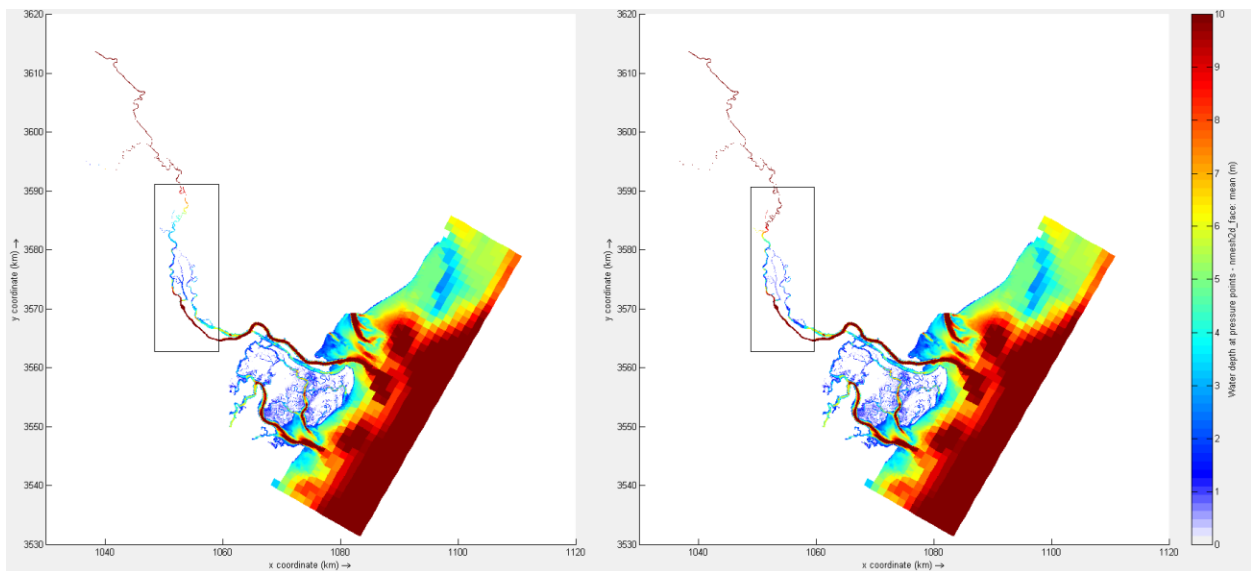


Figure 2. Maximum floodwater depth in Savannah River delta. Simulations of mean sea level and river flow for a return period of (a) 10-year (1413 m<sup>3</sup>/s) and (b) 1000-year (2273 m<sup>3</sup>/s). Black boxes outline differences of floodwater depth in the transitional zone. The

water depth maps created for the lower parts of the transitional zone (wetland) suggest the negligible effect of river discharge on coastal wetland inundation.

How did you test different combinations of W1 and W2 (Weight parameters)? Please clarify.

**Response:** Knowing the condition of  $W1+W2=1$ , we uniformly pick 100 random  $w1$  from the range of 0-1 which results in 100 set of  $w1$  and  $w2$  ( $1-w2$ ) for our calibration. Please refer to [lines 321-322](#) in the revised manuscript.

It is not clear how the parameter of TH is derived. Please clarify.

**Response:** The TH parameter is the result of solving a simple optimization problem by minimizing the total error. We added more information to better explain how to optimize the parameter TH in the revised manuscript. Please refer to [lines 357-359](#).

“To calibrate the binary classifier we minimize the error while searching for the optimum TH value. This means, we use a hundred TH values uniformly picked from the range of  $I_{HD}^{min}$  and  $I_{HD}^{max}$ . For each TH, we use Eq. 2 to generate a binary hazard map and then compare this map with the reference map by calculating the error from Eqs. 3-5.”

The manuscript would be significantly improved by providing more discussion about the broader contribution of the study. (e.g., How coastal planners and managers could benefit from the proposed methodology? How the proposed methodology can be utilized in other coastal regions?)

**Response:** We provided more discussion on the broader impacts of this study and implementation of it in other coastal regions. Please refer to [lines 550-555 and 580-609](#) in the revised manuscript.

“To implement this approach, first, a hydrodynamic model should be set up for the new study area and generate reference inundation maps for different return periods. Access to observed water level data (gauges or HWMs) and flood extent maps from past floods is required to properly calibrate the hydrodynamic model. Then the  $I_{HD}$  index calculated from a DEM is utilized together with the reference maps to provide the hydrogeomorphic threshold operative curves for future floods.”

“Operationally, the Sea, Lake, and Overland Surges from Hurricanes (SLOSH) model (Jelesnianski et al., 1984) is the storm surge model currently used by NWS to perform storm surge forecasting and create probabilistic flood inundation maps for real-time tropical storms (Sea, Lake, and Overland Surges from Hurricanes (SLOSH, 2022)). The feature of SLOSH that makes it the preferred model of the NWS for storm surge forecasting and mapping is the model’s computational efficiency that allows the model to be run as an ensemble (Forbes et al., 2014). However, SLOSH is just one of several modeling options for storm surge modeling and mapping, each possessing strengths and weaknesses associated with their simulations. The inclusion of additional models that can create flood maps of storm surge for a given event should provide an enhanced understanding of the uncertainty of inundation at a given location (Teng et al., 2015). However, the higher computational burden of alternative models, such as Delft3D-FM, tend to preclude their

use in real-time operations and certainly, their use in generating an ensemble necessary for probabilistic flood maps. The methodology we propose in this manuscript may offer the NWS and other agencies a means to utilize alternatives to SLOSH for flood inundation mapping and probabilistic flood inundation mapping on U.S. coastlines. Models such as Delft3D-FM can generate reference maps to train the binary classifier and build the probabilistic operating curves. The probabilistic operative curves would account for the major source of uncertainties and provide a computationally efficient and reliable decision-making tool for coastal planners and floodplain managers. The operative hydrogeomorphic threshold classifiers proposed for real-time coastal flood hazard mapping can be used as an alternative tool for the rapid estimation of hazardous areas during real-time flood events. In an operational mode, water level or meteorological forecasts can be used to estimate the return period of an upcoming coastal flood event and the methodology here can utilize this as an input to perform LCFM flood inundation mapping both deterministically and probabilistically.”

The limitations of the study and the possible enhancements of the proposed methodology should be discussed clearly

**Response:** We have already included three areas of research for future studies. To expand this, we added more text explaining the study limitations and potential areas for future research. Please refer to lines 520-528 in the revised manuscript.

“The proposed hydrogeomorphic index ( $I_{HD}$ ) is the primary data for flood hazard mapping in this study. Thus, the quality of two main inputs of this index, namely the DEM and stream network used to calculate features H and D play a vital role in the overall accuracy of the proposed approach. To obtain maximum accuracy, here we used the best available DEM with the finest spatial resolution of 3 m that includes the bathymetry data. However, considering the limited access to such high-quality DEMs in many areas of the world, it is recommended to evaluate the sensitivity of the proposed approach to lower quality DEMs (e.g. 30 m and 90 m DEMs without bathymetry information) in future studies. Another piece of research can investigate the sensitivity of the proposed approach to the density of the drainage network used for calculating the  $I_{HD}$  index.”

In general here are the areas of research we recommended for future studies:

1. Sensitivity of the hydrogeomorphic index to DEM quality and stream network density (Lines 520-528)
2. Applying the proposed hydrogeomorphic operative curves to inland floods and to other deltas across the US. (Lines 544-550)
3. Improve the flood frequency analysis, considering its uncertainties, incorporating other sources of uncertainties in the modeling to generate probabilistic operative curves (Lines 556-577)
4. A benchmark study that compares the performance of three LCFM methods (Lines 617-620)

1 **Real-time coastal flood hazard assessment using DEM-based**  
2 **hydrogeomorphic classifiers**

3

4

5 Keighobad Jafarzadegan<sup>1</sup>, David F. Muñoz<sup>1</sup>, Hamed Moftakhari<sup>1</sup>, Joseph L Gutenson<sup>2</sup>,  
6 Gaurav Savant<sup>2</sup>, Hamid Moradkhani<sup>1</sup>

7

8 <sup>1</sup> Center for Complex Hydrosystems Research, Department of Civil, Construction, and  
9 Environmental Engineering, University of Alabama, Tuscaloosa, AL

10 <sup>2</sup> US Army Engineer Research and Development Center, Coastal and Hydraulics Laboratory,  
11 Vicksburg, MS, USA

12

13 *Correspondence to:* Keighobad Jafarzadegan [kjafarzadegan@ua.edu](mailto:kjafarzadegan@ua.edu)

14

15 **Key Points**

16• A DEM-based approach is developed for rapid flood hazard assessment in coastal regions.

17• The Height Above Nearest Drainage (HAND) is modified for flood mapping in flat areas.

18• Operative hydrogeomorphic curves are proposed for real-time flood hazard mapping.

19

20

21

22

## 23 Abstract

24 ~~Deltas, estuaries, and wetlands are prone to frequent coastal flooding throughout the world. In~~  
25 ~~addition, a large number of people in the United States have settled in these low lying regions.~~  
26 ~~Therefore, the ecological merit of wetlands for maintaining sustainable ecosystems highlights the~~  
27 ~~importance of flood risk and hazard management in these regions. Typically, hydrodynamic~~  
28 ~~models are used for coastal flood hazard mapping. The huge computational resources required for~~  
29 ~~hydrodynamic modeling and the long running time of these models (order of hours or days) are~~  
30 ~~two major drawbacks that limit the application of these models for prompt decision making by~~  
31 ~~emergency responders.~~ In the last decade, DEM-based classifiers based on Height Above Nearest  
32 Drainage (HAND) have been widely used for rapid flood hazard assessment demonstrating  
33 satisfactory performance for inland floods. The main limitation is the high sensitivity of HAND to  
34 the topography which degrades the accuracy of these methods in flat coastal regions. In addition,  
35 these methods are mostly used for a given return period and generate static hazard maps for past  
36 flood events. To cope with these two limitations, here we modify HAND, ~~and~~ propose a composite  
37 hydrogeomorphic index and develop hydrogeomorphic threshold operative curves for rapid real-  
38 time flood hazard assessment in coastal areas. ~~We also propose the development of~~  
39 ~~hydrogeomorphic threshold operative curves for real-time flood hazard mapping.~~ We select the  
40 Savannah river delta as a testbed, calibrate the proposed hydrogeomorphic index on Hurricane  
41 Matthew and validate the performance of the developed operative curves for Hurricane Irma. The  
42 hydrogeomorphic index is proposed as the multiplication of two normalized geomorphic features,  
43 HAND and distance to the nearest drainage. The calibration procedure tests different combinations  
44 of the weights of these two features and determines the most appropriate index for flood hazard  
45 mapping. Reference maps generated by a well-calibrated hydrodynamic model, Delft3D-FM  
46 model, are developed for different water level return periods. For each specific return period, a

47 threshold of the proposed hydrogeomorphic index that provides the maximum fit with the  
48 relevant reference map is determined. The collection of hydrogeomorphic thresholds developed  
49 for different return periods are used to generate the operative curves. Validation results  
50 demonstrate that the total cells misclassified by the proposed hydrogeomorphic threshold operative  
51 curves (summation of overprediction and underprediction) are less than 20% of the total area. can  
52 rapidly generate flood hazard maps with satisfactory accuracy. The satisfactory accuracy of the  
53 validation results This indicates the high efficiency of our proposed methodology for fast and  
54 accurate-reliable estimation of hazard areas for an upcoming coastal flood event which can be  
55 beneficial for emergency responders and flood risk managers.

## 56 **1. Introduction**

57 Densely populated coastal areas are some of the most productive ecosystems on Earth. Coastal  
58 wetlands provide important services to society, including flood attenuation, water storage, carbon  
59 sequestration, nutrient cycling, pollutant removal, and wildlife habitat (Barbier, 2019; Land et al.,  
60 2019; Wamsley et al., 2010). Characterizing the hydrological processes unique to coastal areas is  
61 tremendously important for ensuring the sustainability of these ecosystem services. Endangered  
62 coastal ecosystems are threatened by anthropogenic effects, including direct impacts of human  
63 activities (i.e. urbanization and navigational development) or indirect impacts (e.g. sea level rise  
64 (SLR), and hydroclimate extremes (e.g. floods) exacerbated by climate change (Alizad et al., 2018;  
65 Kirwan and Megonigal, 2013; Wu et al., 2017). Nearly 70% of global wetlands have been lost  
66 since the 1900s and rates of wetland loss have increased by a factor of 4-four in the late 20<sup>th</sup> and  
67 early 21<sup>st</sup> century (Davidson, 2014). Urbanization hinders wetland migration toward upland areas  
68 in an effort to cope with rising water levels (WLs) (Schieder et al., 2018). Likewise, moderate to  
69 high Relative Sea Level Rise (RSLR) rates can influence the fate of sediments and nutrient

70 availability to coastal wetlands (Schile et al., 2014); and eventually transform low marsh regions  
71 into open water or mudflat areas (Alizad et al., 2018). SLR and navigational development can alter  
72 the tidal regime and long-wave propagation characteristics inside estuaries/bays and ~~so~~  
73 subsequently change the flooding inundation patterns (Familkhalili et al., 2020; Khojasteh et al.,  
74 2021a, b). Similarly, hurricane impacts can create interior ponds, trigger shoreline erosion, and  
75 denude marshes (Morton and Barras, 2011). People and assets located in low-lying coastal regions  
76 and river deltas are frequently exposed to compound flooding. Challenges for flood hazard  
77 assessment unique to these systems include compounding effects of multiple flooding  
78 mechanisms, complex drainage systems with relatively low slopes, and periodically saturated  
79 soils. ~~It~~ It is expected that between 0.2-4.6% of the global population may be exposed to coastal  
80 flooding if no strategic adaptation takes place (Kulp and Strauss, 2019).

81 Efficient ~~lood~~-risk reduction strategies require accurate real-time assessment of flood~~ing~~ hazards  
82 (Gutenson, 2020; USGS Surface Water Information, 2021). ~~In order to~~ To simulate the coastal flood  
83 hazard in wetlands, two-dimensional (2D) hydrodynamic models are commonly used for flood  
84 inundation mapping, as they allow for simulating complex oceanic, hydrological, meteorological,  
85 and anthropogenic processes based on process-based numerical schemes. The advanced circulation  
86 model (ADCIRC) (Luettich et al., 1992), DELFT3D (Roelvink and Banning, 1995), and  
87 LISFLOOD-FP (Bates et al., 2010) are among the most commonly used 2D hydrodynamic models  
88 for coastal flood hazard assessment in low-lying areas at local and regional scales (Bates et al.,  
89 2021; Muis et al., 2019; Thomas et al., 2019). Nonetheless, hydrodynamic modeling approaches  
90 require huge computational resources to conduct flood hazard assessments at a large scale. This is  
91 even more challenging when emergency responders need timely flood risk information at a  
92 desirable accuracy and resolution on a real-time basis. Therefore, while 2D hydrodynamic models

93 are still a key component in many frameworks for detailed analyses of the flood hazard, the use of  
94 low-complexity flood mapping (LCFM) methods is essential for the preliminary estimation of  
95 areas exposed to flooding in a short time. Applying LCFM methods together with detailed  
96 hydrodynamic models provide a more comprehensive set of information for emergency responders  
97 and improve the efficiency of flood risk management in practice.

98 The advent of Digital Elevation Models (DEMs) has led to the development of a series of GIS-  
99 based LCFM methods for rapid estimation of flood hazard in the last couple of decades (Afshari  
100 et al., 2018; Dodov and Fofoula-Georgiou, 2006; Manfreda et al., 2011; McGlynn and  
101 McDonnell, 2003; McGlynn and Seibert, 2003; Nardi et al., 2006; Samela et al., 2016; Teng et al.,  
102 2015; Williams et al., 2000). Among these methods, binary classification of a hydrogeomorphic  
103 raster has been shown to be an efficient approach for reliable delineation of floodplains (Degiorgis  
104 et al., 2012; Manfreda et al., 2014). In a binary hydrogeomorphic classification approach, the study  
105 area is examined as a grid of cells, then a threshold of a hydrogeomorphic feature, typically  
106 calculated from a DEM, is chosen. Comparing the hydrogeomorphic feature value of cells with  
107 the threshold, the entire study area is classified into flooded and non-flooded cells.

108 The Federal Emergency Management Agency (FEMA) provides flood hazard maps across the  
109 United States. These maps, also referred to as Flood Insurance Rate Maps (FIRMs) identify flood-  
110 prone areas corresponding to specific return periods. While these hazard maps provide useful  
111 information for a few recurrence intervals, they are no longer reliable for extreme flood events  
112 characterized by lower frequencies or longer return periods. In 2015, the National Water Center  
113 Innovators Program initiated the national flood interoperability experiment (NFIE) for real-time  
114 flood inundation mapping across the United States (Maidment, 2017; Maidment et al., 2014). The  
115 plan highlighted the tendency for event-based flood mapping which is more valuable and practical

116 for emergency response and warning systems. Unlike past DEM-based methods that mostly  
117 focused on flood hazard mapping, Zheng et al., (2018b) proposed the development of DEM-based  
118 synthetic rating curves for real-time flood inundation mapping. In most current, real-time flood  
119 mapping methods, the forecasted river flows and/or water surface elevation are typically fed into  
120 flood inundation libraries to simulate the upcoming flood inundation areas (IWRSS, 2015, 2013;  
121 Maidment, 2017; Wing et al., 2019; Zheng et al., 2018a). The computationally intensive and time-  
122 consuming nature of detailed hydrodynamic models to numerically route flood waves typically  
123 restricts their usage in supporting emergency response activities (Gutenson et al., 2021;  
124 Longenecker et al., 2020).

125 An LCFM method based on Height Above Nearest Drainage (HAND) has been widely used and  
126 recognized as one of the best classifiers for identifying flood hazard areas (Degiorgis et al., 2012;  
127 Jafarzadegan et al., 2018; Jafarzadegan and Merwade, 2019; McGrath et al., 2018; Samela et al.,  
128 2017; Zheng et al., 2018a). The performance assessment of HAND classifiers in different  
129 topographic settings suggests, despite an acceptable performance in most locations, the accuracy  
130 of hazard maps is significantly lower in low-lying coastal regions (Jafarzadegan and Merwade,  
131 (2017) and Samela et al., (2017)). While the majority of DEM-based flood hazard mapping  
132 methods have been developed and tested for inland floods, access to an appropriate DEM-based  
133 method for coastal flooding is lacking in the literature. Since coastal flooding occurs rapidly and  
134 the time for hydrodynamic modeling and designing flood mitigation strategies is limited especially  
135 in data-scarce regions, efficient DEM-based approaches can be significantly beneficial for  
136 emergency and response-related decision-makers.

137 The overarching goal of this study is to propose a DEM-based LCFM method for coastal wetlands,  
138 estuaries, and deltas. To our knowledge, this is the first study that investigates the application of

139 hydrogeomorphic binary classifiers for flooding in semi-flat coastal zones. We modify the HAND  
140 commonly used for riverine inland flooding (Degiorgis et al., 2013; Jafarzadegan et al., 2020;  
141 Samela et al., 2017) and propose a composite hydrogeomorphic index for tidally-influenced  
142 coastal regions. We enhance the applicability of the proposed method by developing  
143 hydrogeomorphic threshold operative curves for coastal flood hazard mapping. Unlike previous  
144 studies that rely on binary classifiers for specific return periods, the operative curves here offer a  
145 unique opportunity for rapid assessment of hazardous areas in real-time. These curves have  
146 substantial benefits for emergency responders when wetlands are prone to coastal flooding.

## 147 **2. Study area and data**

148 We study the Savannah River delta located ~~in the Southeast United States, at the border of~~ Georgia  
149 ~~and South Carolina in the southeast United States~~ (Figure 1a). ~~The Savannah River originates at~~  
150 ~~the confluence of Tulagoo and Seneca rivers and drains the Lower Savannah watershed~~  
151 ~~(HU08\_03060109) comprising an area of 2603.96 km<sup>2</sup>.~~ The morphology of this region is relatively  
152 complex due to the existence of a braided river followed by a dense drainage network of interior  
153 rivers and tidal creeks. ~~The average slope, length, and annual discharge of the Savannah River are~~  
154 ~~0.00011 m/m, 505 km, and 320 m<sup>3</sup>/s, respectively~~ (Carlston, 1969). ~~Moreover, the river~~  
155 ~~bathymetry was deepened up to 12 m for increasing the capacity of cargo transportation~~ (U.S.  
156 Army Corps of Engineers, 2017). ~~This region is mostly characterized by its unique ecology,~~  
157 ~~including vast wetlands and saltmarsh ecosystems.~~ ~~We obtain detailed drainage network data~~  
158 ~~including river streams, tidal channels, and creeks within wetland areas from the U.S. National~~  
159 ~~Wetlands Inventory (<https://www.fws.gov/wetlands/data/Mapper.html>).~~

160 To simulate the flood hazard in this region, a mesh boundary encompassing the Savannah River  
161 delta, surrounding areas, and a portion of the Atlantic Ocean is generated (Figure 1b). Two U.S.

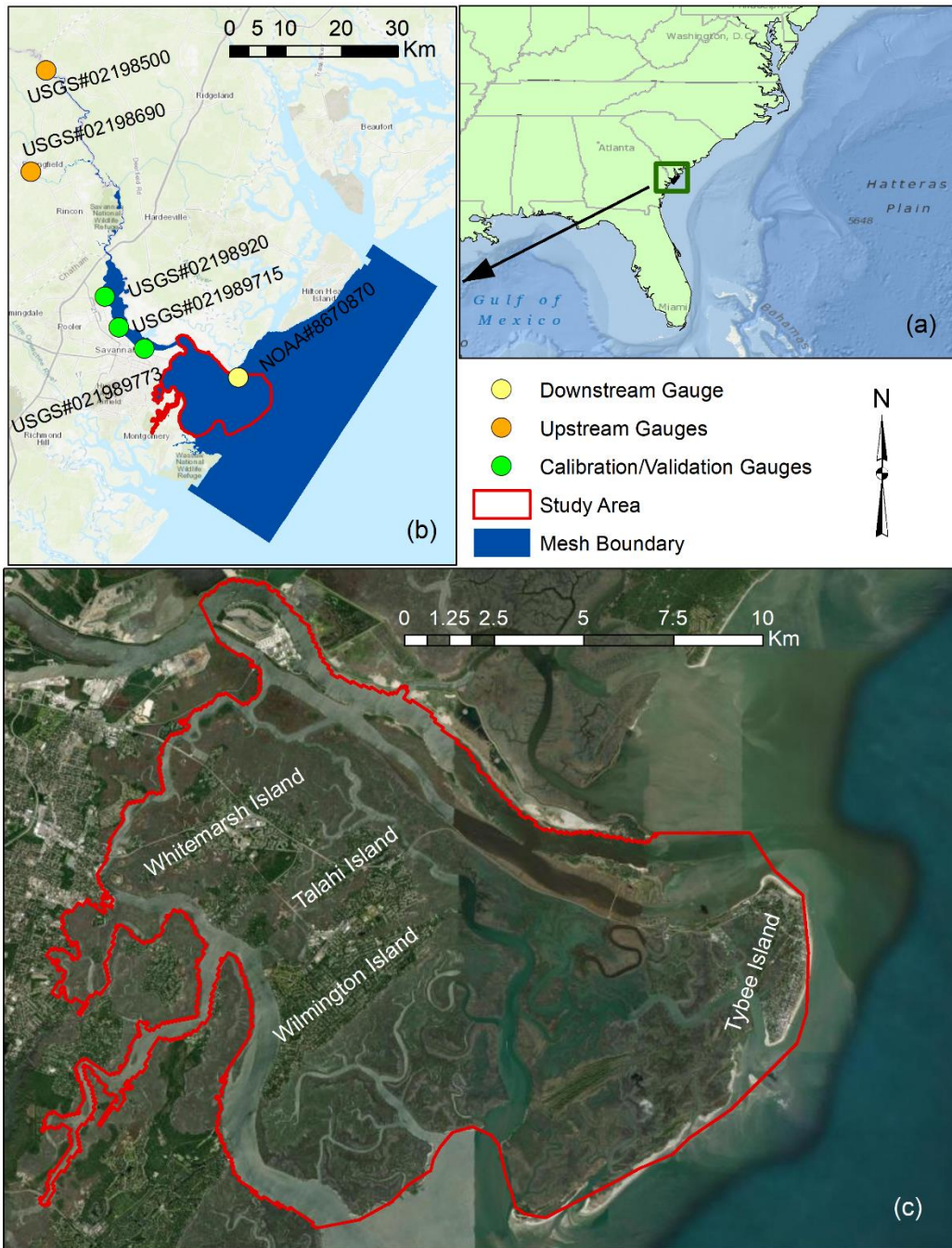
162 Geological Survey (USGS) gauges, located at the Savannah River (#02198500, #02198690) and  
163 the Fort Pulaski station of the National Oceanic and Atmospheric Administration (NOAA) are  
164 used as upstream and downstream boundary conditions of the hydrodynamic model, respectively.  
165 Fort Pulaski station (NOAA – 8670870) counts with an 85-year length of records (since 1935) that  
166 enables a proper characterization of coastal flooding for design levels at lower frequencies or  
167 relatively large return periods. We select this region as a testbed because of 1) frequent coastal  
168 flooding induced by large semidiurnal tidal amplitudes at the estuary mouth (Cowardin et  
169 al., 2013) and 2) exposure of more than twenty thousand people settled in four developed areas,  
170 the Whitemarsh, Talahi, Wilmington, and Tybee Islands located in this region (Figure 1c).

171 The high-resolution DEM used as the base of our proposed hydrogeomorphic index is a 3 m light  
172 detection and ranging (LiDAR) that includes topographic and bathymetric (topobathy) data. This  
173 dataset has been developed by the NOAA's National Centers for Environmental Information  
174 (NCEI) and is available at the NOAA's Data Access Viewer repository  
175 (<https://coast.noaa.gov/dataviewer/>). The topobathy data was further corrected for wetland  
176 elevation error using the DEM-correction tool developed by Muñoz et al., (2019) ~~in order to~~  
177 minimize vertical bias errors commonly found in LiDAR-derived coastal DEMs (Alizad et al.,  
178 2018; Medeiros et al., 2015; Rogers et al., 2018). The vertical and horizontal accuracy of the DEM  
179 are 50 and 100 cm, respectively and its vertical datum is the North American Vertical Datum 1988  
180 (NAVD88). Land cover maps are obtained from the 2016 National Land Cover Database (NLCD)  
181 available at (<https://www.mrlc.gov/>). River discharge and WL records are obtained from the USGS  
182 (<https://maps.waterdata.usgs.gov/mapper/index.html>) and NOAA  
183 (<https://tidesandcurrents.noaa.gov/>), respectively. In addition, post-flood high water marks  
184 (HWMs) of Hurricane Irma and Matthew are obtained from the USGS Flood Event Viewer

185 platform (<https://stn.wim.usgs.gov/FEV/>). These high-water marks are used for calibration and  
186 validation of the Savannah model in Delft3D-FM. Specifically, we used the 2021 Delft3D-FM  
187 suite package to model the complex interactions between riverine, estuarine, and intertidal flat  
188 hydrodynamics. The suite package can provide detailed information ofn water level, flow rates,  
189 and velocity (Delft3D Flexible Mesh Suite - Deltares, 2021).

190

191

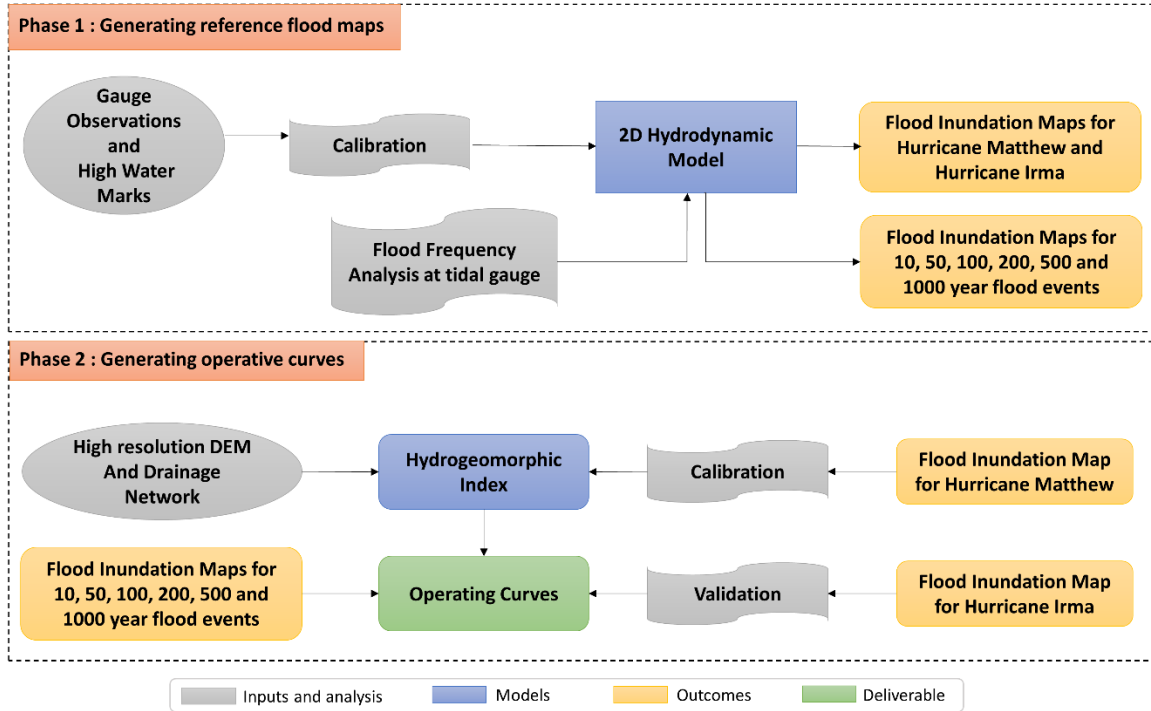


194 **Figure 1.** Map of the study area and mesh boundary of the hydrodynamic model. (a) the geographic  
 195 location of the study area in the southeast U.S., (b) The mesh boundary used by the hydrodynamic  
 196 model (blue) for flood inundation mapping as well as the location of upstream (orange),

197 downstream (yellow), and calibration/validation (green) gauges, and (c) the boundary of Savannah  
198 wetlands used as the case study along with urbanized areas. (ESRI 2018)

### 199 **3. Methods**

200 We propose a DEM-based LCFM approach for the rapid assessment of flood hazard areas in real-  
201 time. The proposed approach consists of two phases (Figure 2). In phase 1, a 2D hydrodynamic  
202 model is calibrated based on observed WLs at USGS gauges and HWMs that are available during  
203 Hurricane Matthew in 2017. We then use the calibrated hydrodynamic model to generate a flood  
204 inundation map that serves as a reference map in the next phase. In addition, for flood frequency  
205 ~~analysis~~analyses, we perform block maxima sampling approach to select the annual WL maxima  
206 at Fort Pulaski station. The selected samples are then used to estimate ~~return levels~~WLs for six  
207 return periods of 10, 50, 100, 200, 500, and ~~1000-year~~1000-year floods. Using these estimated  
208 WLs as the main boundary conditions of the hydrodynamic model, we also generate six flood  
209 inundation maps corresponding to these return periods. In phase 2, we use a high-resolution DEM  
210 together with the drainage network data to calculate the hydrogeomorphic index. Subsequently,  
211 the flood inundation map generated for Hurricane Matthew in phase 1, is used as a reference map  
212 to calibrate the hydrogeomorphic index. Then, the calibrated index uses the flood inundation maps  
213 provided for different return periods in phase 1 to develop the operative curves. These curves form  
214 the basis for the rapid assessment of flood hazard areas for any upcoming coastal flood event in  
215 the future. To validate the effectiveness and reliability of the developed operative curves, we use  
216 them to identify hazard areas corresponding to Hurricane Irma, and then we compare their  
217 accuracy with the reference map provided by the hydrodynamic model for this flood event. In the  
218 following sections, we further explain the hydrodynamic model, flood frequency analysis, and  
219 hydrogeomorphic method, respectively.



221

222 **Figure 2.** Flowchart of the proposed approach for generating hydrogeomorphic threshold  
 223 operative curves. In Phase 1, the 2D hydrodynamic model is calibrated and generates the required  
 224 reference maps for the next phase. In Phase 2, the reference maps are used in conjunction with the  
 225 hydrogeomorphic index to generate the operative curves for fast and real-time coastal flood hazard  
 226 assessment.

227 **3.1 Hydrodynamic Model**

228 **3.1.1 Model setup**

229 We use the 2019 Delft3D-FM suite package (Deltares, 2019) to model the complex riverine,  
 230 estuarine, and intertidal flat hydrodynamics in the Savannah River delta and wetland regions. The  
 231 suite package has been used in similar coastal studies characterized by vast wetland regions with  
 232 satisfactory results (Fagherazzi et al., 2014; Kumbier et al., 2018; Sullivan et al., 2019). Moreover,  
 233 the model developed for Savannah has been used in other studies to simulate extreme and non-  
 234 extreme events including Hurricane Matthew that hit the southeast Atlantic Coast in October 2016

235 (Muñoz et al., 2021, 2020). The 2D hydrodynamic model comprises nearly 85 km of the Savannah  
236 River extending from Fort Pulaski station (NOAA – 8670870) at the coast up to Clyo station  
237 (USGS – 02198500) and cover an area of 1178 km<sup>2</sup> approximately. The model consists of an  
238 unstructured triangular mesh to ensure a correct representation of geomorphological settings  
239 including sinuous and braided river waterways and relatively narrow tidal inlets. Furthermore, the  
240 mesh has a spatially varying cell size ranging from 1.5 m in the upstream riverine area, 10 m over  
241 wetland regions, 120 m along the coast, and up to 1.4 km over the Atlantic Ocean (Figure 1b).

### 242 **3.1.2 Model calibration**

243 For calibration purposes, the model was forced with time series of river flow obtained from Clyo  
244 station as an upstream boundary condition (BC), coastal WL from Fort Pulaski station as a  
245 downstream BC, and with spatially varying Manning’s roughness values ( $n$ ) classified into open  
246 water, wetland, urban, and riverine areas. The optimal (or calibrated) set of  $n$ -values were~~s~~-was  
247 inferred from 200 model simulations of Hurricane Matthew, as this event reported the highest peak  
248 WL at Fort Pulaski station since the year 1935 (2.59 m w.r.t. NAVD88). Each simulation was  
249 conducted in a high-performance computing system and included a one-month warm-up period  
250 and a unique set of  $n$ -values for each land cover generated with the Latin Hypercube Sampling  
251 (LHS) technique (Helton and Davis, 2003). The advantage of LHS over traditional Monte Carlo  
252 approaches is that the former results in a denser stratification over the range of each sampled  
253 parameter and is therefore superior to random sampling. LHS leads to more stable results that are  
254 closer to the true probability density function of the parameter and has been used in similar studies  
255 (Jafarzadegan et al., 2021; Muñoz et al., 2022). The range of  $n$ -values was derived from pertinent  
256 literature and included hydrodynamic modeling and open channel flow studies (Arcement and  
257 Schneider, 1989; Chow Ven, 1959; Liu et al., 2019). The set of values achieving both the lowest

258 Root Mean Square Error (RMSE) ~~and highest correlation coefficient ( $R^2$ )~~ and highest Kling-Gupta  
259 Efficiency (KGE) around the peak WL (e.g., 7-day window) was selected as the optimal one and  
260 further used for coastal flood simulations. KGE is a robust evaluation metric that accounts for  
261 correlation, bias, and the ratio of variances and can take values between  $-\infty$  and 1 (Gupta et al.,  
262 2009). An efficiency of 1 indicates a perfect match between model simulations and observations.  
263 In addition to those metrics, we evaluate the model's performance using the Nash-Sutcliffe  
264 Efficiency (NSE) and Mean Absolute Bias (MAB). NSE measures the relative magnitude of the  
265 error variance of model simulations compared to the variance of observational data (Nash and  
266 Sutcliffe, 1970). NSE ranges between  $-\infty$  to 1, where an efficiency of 1 indicates a perfect match.  
267 MAB quantifies the bias of model simulations with respect to observational data. MAB of 0  
268 suggests an absence of bias in the simulation. The calibrated  $n$ -values used in ~~this~~ the Savannah  
269 model are: open water ( $n = 0.027$ ), wetland ( $n = 0.221$ ), urban ( $n = 0.03$ ), and  
270 downstream/upstream riverine areas ( $n = 0.037$  and  $n = 0.086$ , respectively).

### 271 3.2 Flood Frequency Analysis

272 Preliminary model simulations indicate a negligible influence of river flow on coastal wetland  
273 inundation as compared to storm surge ~~at~~ on ~~the~~ the Wassaw Sound, Wilmington, and Tybee islands  
274 (Figure 1c). This can be explained by the proximity of the islands to the Atlantic Ocean as well as  
275 freshwater runoff regulation and flood controls by three large dams located upstream of the Clio  
276 station (USGS – 02198500), namely J. Strom Thurmond, Richard B. Russell, and Hartwell  
277 (Zurqani et al., 2018). In addition, bivariate statistical analysis via copulas suggests no significant  
278 correlation between river flow at Clio station (USGS - 02198500) and coastal water levels at Fort  
279 Pulaski station (NOAA - 8670870). The latter was also reported in Ghanbari et al., (2021) and  
280 Muñoz et al., (2020). Furthermore, our analysis demonstrated that high river flow does not affect

281 the inundation area in wetlands areas. This indicates that flood inundation is highly dominated by  
282 coastal forcing as tides propagate into the Savannah River and lead to flow reversal at upstream  
283 gauge stations (see Figure 1 below). The high proximity of wetlands to the Atlantic Ocean shows  
284 that the transitional zone, i.e., the area affected by both coastal and inland drivers, is located  
285 upstream of Port Wentworth station (USGS - 02198920) where the Savannah river trifurcates into  
286 the Back River, Middle River, and Front River. Considering the dominant role of sea water level  
287 in coastal flooding as well as the negligible effect of river discharge on wetland inundation from  
288 the previous analyses, we can justify the proposed univariate flood frequency analysis. We,  
289 therefore, conduct a univariate flood frequency analysis based on annual block maxima sampling  
290 of WLs observed at the Fort Pulaski station (~~NOAA—8670870~~). We use the 'allfitdist' tool in  
291 MATLAB to find the best parametric probability distribution fit to the data, based on Maximum  
292 Likelihood, Bayesian information criterion (BIC), or Akaike information criterion (AIC).

### 293 **3.3 Hydrogeomorphic index**

294 Among different hydrogeomorphic features used for flood hazard mapping, HAND (sometimes  
295 also referred to as feature  $H$ ) has been widely used as one of the best indicators of floodplains.  
296 However, due to the weakness of this feature for proper characterization of floodplains in flat  
297 regions and coastal areas, here we develop a composite hydrogeomorphic index that considers  $H$   
298 as well as the distance to the nearest drainage ( $D$ ). Although the overall performance of feature  $D$   
299 is less than  $H$  in most case studies (Degiorgis et al., 2012; Manfreda et al., 2015a; Samela et al.,  
300 2016), feature  $D$  can be a better descriptor of floodplains in highly flat regions according to the  
301 study conducted by Samela et al., (2017). In another study, Gharari et al., (2011) proposed a  
302 composite index by multiplying both features  $H$  and  $D$  and demonstrated that  $H$  is a better feature  
303 compared to the case that both features are used for landscape classification. The main drawback

304 of their proposed index was that they used the same weights for both features which result in  
305 degrading the classification performance. To overcome the limitation of the proposed index and  
306 to consider the key role of feature  $D$  in flat areas, we maintain feature  $D$  in our composite index  
307 and add different weights to  $H$  and  $D$  using Eq. 1 as follows:

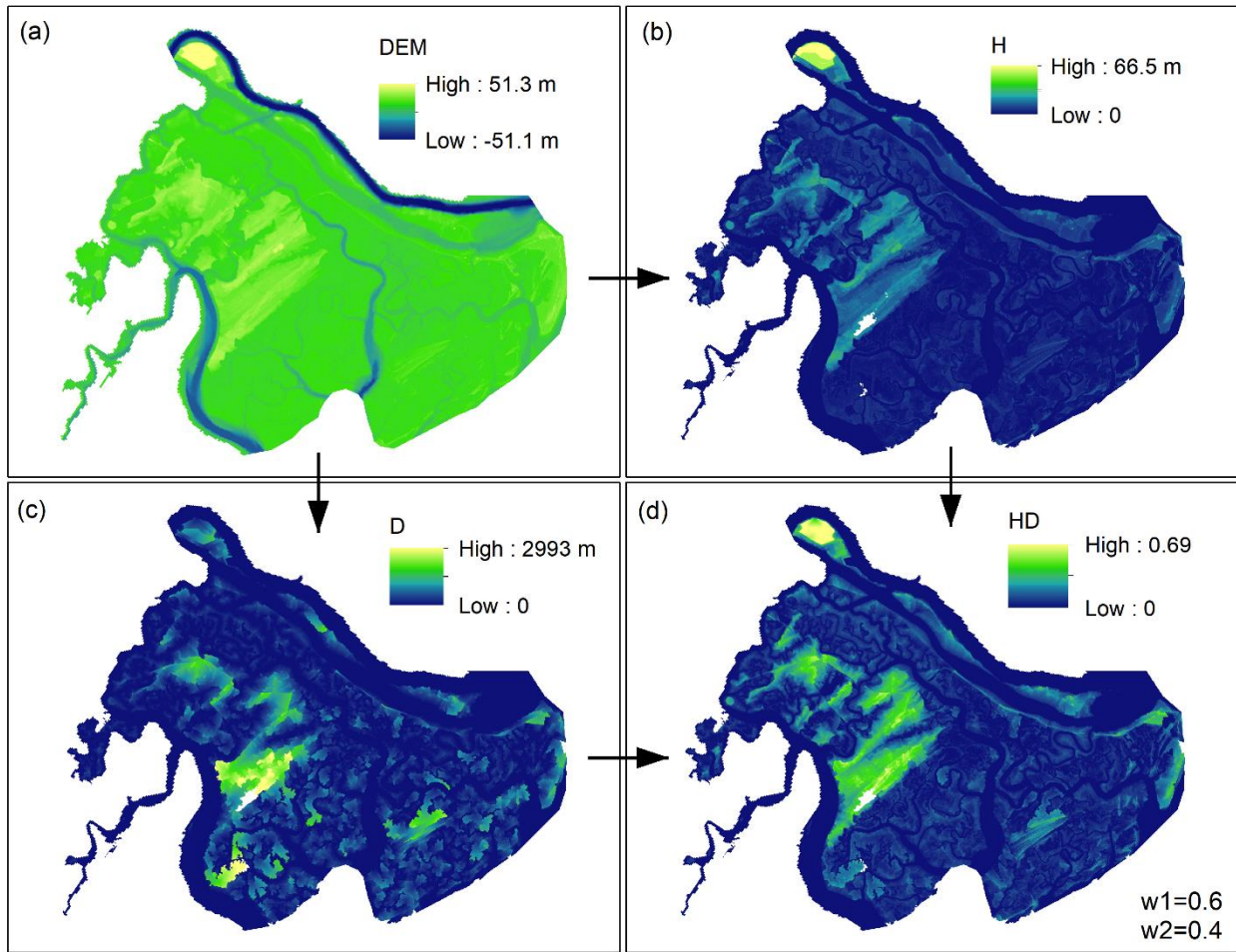
$$308 \quad I_{HD} = \left(\frac{H}{H_{max}}\right)^{w1} \times \left(\frac{D}{D_{max}}\right)^{w2} \quad \text{where} \quad w1 + w2 = 1 \quad (1)$$

309 In Eq.1,  $H_{max}$  and  $D_{max}$  denote the maximum value of raster  $H$  and  $D$  used for normalizing the  
310 hydrogeomorphic index whereas  $w1$  and  $w2$  refer to the weights of feature  $H$  and  $D$ , respectively.  
311 The conditional equation of  $w1 + w2 = 1$  helps lower the computational burden of the calibration  
312 procedure by reducing the number of unknown parameters from two to one. Figure 3 illustrates an  
313 example of calculating the  $I_{HD}$  index with a given set of weights ( $w1=0.6$  and  $w2=0.4$ ) for the  
314 study area. Using a high-resolution coastal DEM (Figure 3a), raster  $H$  and  $D$  are calculated  
315 (Figures 3b and 3c). Considering a DEM with  $N$  cells, the main step is to find a coordinate matrix  
316 that indicates the location of the nearest stream cell to each grid cell. Knowing this matrix and the  
317 number of cells required to cross the nearest stream cell, the feature  $D$  is calculated. The coordinate  
318 matrix can also be used in conjunction with the DEM to calculate the feature  $H$ . ~~In order to~~  
319 calculate the ~~hydrogeomorphic index~~  $I_{HD}$  index, the weights in Eq. 1 are calibrated using a  
320 reference flood hazard map obtained from hydrodynamic simulation (e.g., Hurricane Matthew).  
321 We tested ~~different a hundred~~ combinations of weight parameters ( $w1$  and  $w2 = 1 - w1$ ),  
322 derived from random generation of 100  $w1$  in the range of (0-1), to find the importance of features  
323  $H$  and  $D$ , and then finalized the  $I_{HD}$  ~~hydrogeomorphic~~ index with known parameters for future  
324 flood hazard mapping. We further validated the weight parameters ~~with-through the~~ simulations  
325 of Hurricane Irma.

326

327

328



329

330 **Figure 3.** The required steps for calculating the proposed hydrogeomorphic index. A high-  
331 resolution coastal DEM (3 m) is used as the source data to (a) generate the Height Above Nearest  
332 Drainage ( $H$ ) and the Distance to the nearest Drainage ( $D$ ), respectively (b, c). Using Eq. 1, the  
333 normalized features  $H$  and  $D$  are multiplied with different weights to generate the  $I_{HD}$   
334 hydrogeomorphic index (d).

### 335 3.4 Binary classifiers for flood hazard mapping

336 Considering the study area as a grid of cells, a binary classifier assigns a value of zero or one to  
337 each cell and generates a map of two different classes. In flood hazard mapping, the common  
338 approach is to define a threshold on a hydrogeomorphic index (e.g.  $I_{HD}$ ) and use the following if-  
339 and-else rule for the classification:

$$340 \quad f(i) = \begin{cases} 1 & I_{HD}^i \leq TH \\ 0 & I_{HD}^i > TH \end{cases} \quad (2)$$

341 where  $f(i)$  and  $I_{HD}^i$  denote the label of flood hazard map and the proposed hydrogeomorphic  
342 index value at cell  $i$ , respectively, and  $TH$  denotes the threshold of the hydrogeomorphic classifier  
343 that should be calibrated. The flood hazard map generated with the binary classifier is compared  
344 with a binary reference hazard map, and the rate of true positive ( $rtp$ ), rate of false positive ( $rfp$ ),  
345 and *error* are calculated as follows (Jafarzadegan and Merwade, 2017):

$$346 \quad rtp = \frac{\text{True positive instances}}{\text{Total positives}} \quad (3)$$

$$347 \quad rfp = \frac{\text{False positive instances}}{\text{Total negatives}} \quad (4)$$

$$348 \quad \text{error} = rfp + (1 - rtp) \quad (5)$$

349 In binary classification, positive and negative refer to a value of one and zero, respectively. True  
350 positive instances are those positive cells that are correctly predicted by the classifier and false  
351 positive instances represent those negative cells that are wrongly classified as positive. The *error*,  
352 reflecting all cells that are wrongly predicted by the classifier, is a commonly-used measure for  
353 validating the performance of binary classifiers for flood hazard mapping. Another useful

354 performance measure to validate the binary classifier is the area under the curve (AUC) of the  
355 Receiver Operating Characteristic (ROC) graph proposed by Fawcett, (2006).

356 To calibrate the binary classifier we minimize the *error* while searching for the optimum *TH* value.

357 This means, we use a hundred *TH* values uniformly picked from the range of  $I_{HD}^{min}$  and  $I_{HD}^{max}$ . For  
358 each *TH*, we use Eq. 2 to generate a binary hazard map and then compare this map with the  
359 reference map by calculating the error from Eqs. 3-5. In this optimization problem, the reference

360 flood hazard map used for calculating the *error* is the key input that should be further described.

361 The flood inundation maps generated by the hydrodynamic model indicate WLs at different cells

362 in different time steps and should be converted to a single binary map. A common approach used

363 for inland floods is to find the maximum inundation area over the entire flooding period and then

364 assign all cells with zero WL to “dry” or “non-flooded” and other cells with positive values as

365 “wet” or “flooded”. In delta estuaries and coastal regions nearby the ocean, however, almost all

366 cells can be flooded with small WL values. Therefore, after finding the maximum inundation over

367 the flooding period, we use another set of binary labels as “low hazard” vs “high hazard” and

368 define the hazard depth cutoff (HDC) as a threshold used to convert a continuous map of WL to a

369 binary map with only two labels. Depending on the HDC used for distinguishing low from high

370 hazard regions, the reference flood map is changed which results in a different calibrated *TH*. In

371 addition to HDC, the intensity of the flood event shown with the return period (~~T~~) also changes

372 the reference flood hazard map. Therefore, the calibrated parameter *TH* is a function of both HDC

373 and T and the main goal of this study is to provide operative curves showing the variation of *TH*

374 with these two factors. We run the hydrodynamic model for 6 different return periods of 10, 50,

375 100, 200, 500, and 1000 year events and then convert the WL maps to binary maps using 21 HDC

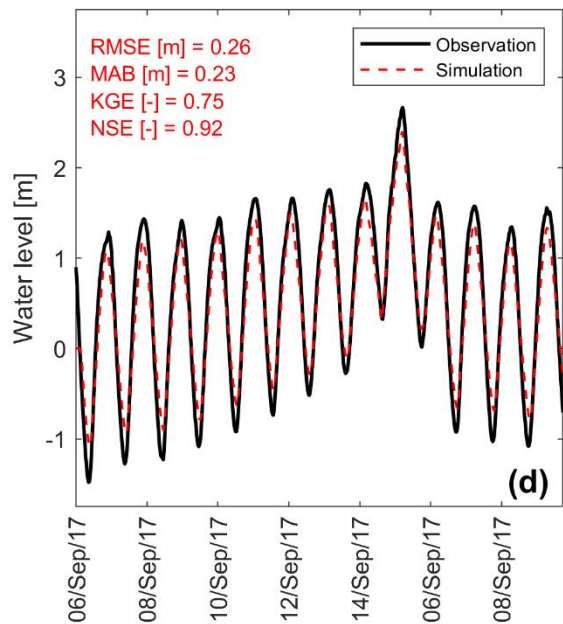
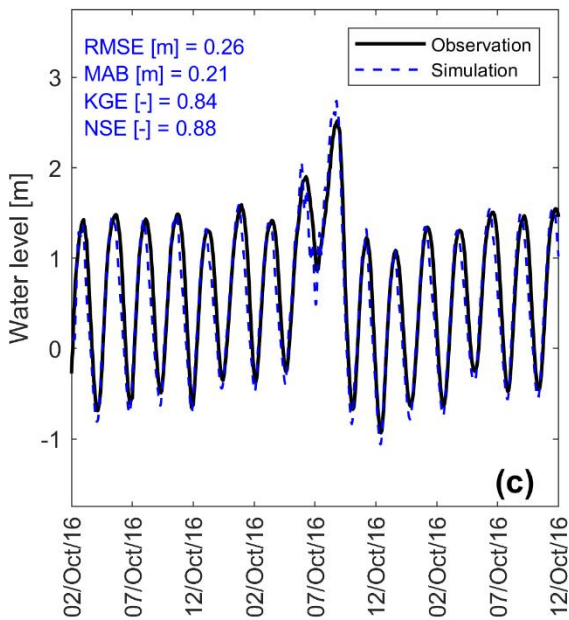
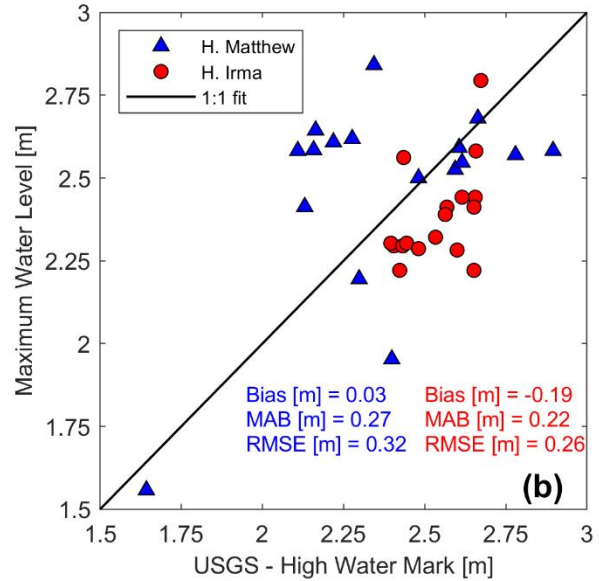
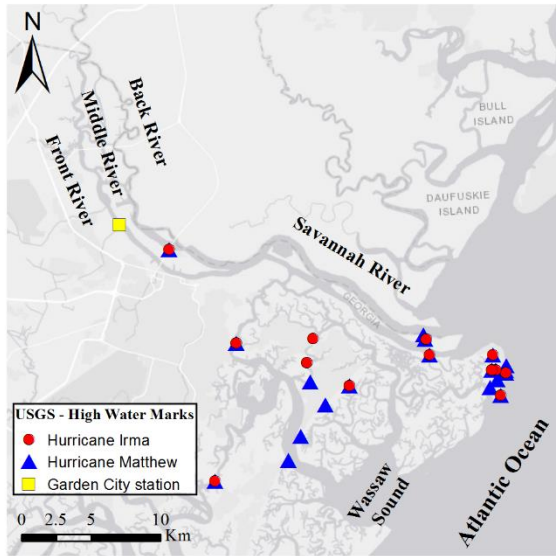
376 resulting from 0.1 increments in the range of 0-2 m. The binary classification and calibration of

377 *TH* are performed for different reference maps generated from various combinations of T and  
378 HDC.

#### 379 **4. Results**

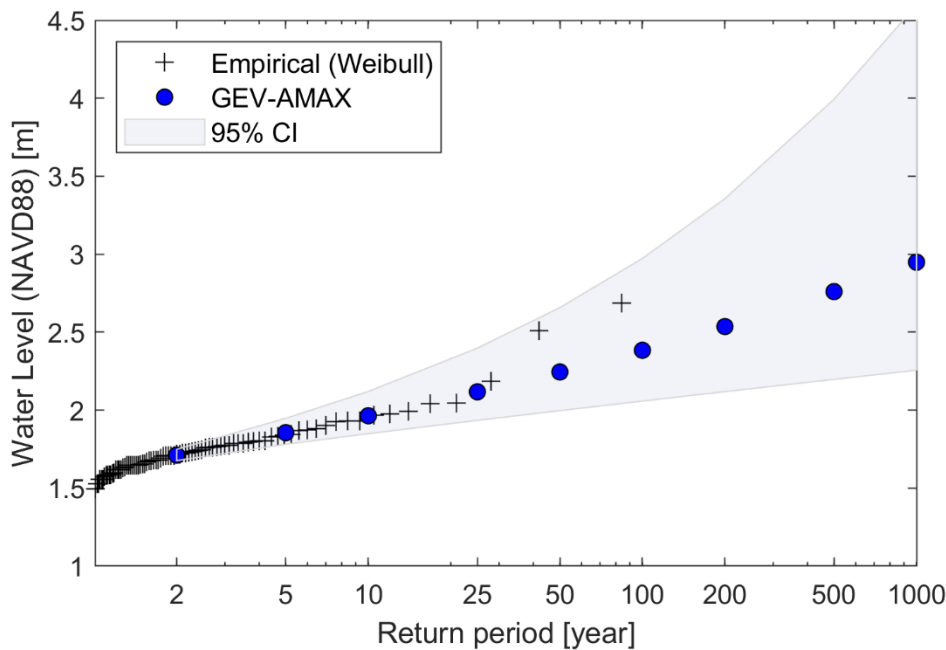
380 A comprehensive calibration and validation of the Savannah River model is shown in Figure 4.  
381 This step is crucial to ensure that the flood hazard maps provided by the model are reliable enough  
382 to be used as the reference of the hydrogeomorphic method. We assess the performance of the  
383 model by first comparing simulated and observed WLs at four USGS stations along the Savannah  
384 River (Figure 1b, green circles). For convenience, we only present simulated and observed WLs  
385 of Hurricane Matthew and Irma at Garden City (Figure 4c and 4d, respectively) located at ~29.5  
386 km from the river mouth (Figure 4a, yellow square). The results of the remaining stations are  
387 included in the supplementary material (Figure S1). ~~The RMSE and MAEB remain below 30 cm~~  
388 ~~and 25 cm whereas KGE and NSE and R<sup>2</sup> of the gauges stations remain below 30 cm and~~  
389 ~~above achieve values above 0.90, 0.75 and 0.85~~, respectively, for the two hurricane events, which is  
390 reflective of satisfactory model performance. Overall, the magnitude and timing of the highest  
391 peak WL observed during the hurricanes are well captured by the Savannah River model. To  
392 further evaluate the model performance in coastal flood propagation analysis, we compare  
393 maximum WLs resulting from model simulations with the USGS HWMs collected in urban and  
394 surrounding wetland areas (Figure 4b). The 1:1 line represents a perfect fit between simulated and  
395 observed maximum WLs and helps visualize overestimation (above the 1:1 line) and  
396 underestimation of the model. Similarly, the evaluation metrics indicate a satisfactory performance  
397 of the model with a slightly over- and underestimation during Matthew and Irma. Moreover, the  
398 model achieves a relatively small RMSE (< 35 cm) ~~and MAE (< 30 cm)~~.

399



402 **Figure 4.** Calibration and validation of the Savannah Delft3D-FM model. (a) Location of high-  
403 water marks (HWMs) in the Savannah River delta for Hurricane Mathew (blue triangles) and  
404 Hurricane Irma (red circles). (b) Comparison between simulated maximum water levels (WLs)  
405 and HWMs in Savannah. (c and d) Time series of simulated and observed WLs at Garden station  
406 for Hurricane Mathew and Hurricane Irma, respectively.

407 To generate boundary conditions for coastal flood modeling simulations associated with the  
408 proposed return periods, we perform flood frequency analysis of coastal WL at the Fort Pulaski  
409 station (in Figure 5) located at the mouth of the Savannah River (Figure 1b, yellow circle). In this  
410 study, we select Generalized Extreme Value (GEV) because of its smallest estimated BIC  
411 compared to other parametric distributions available at the [Matlab](#) 'allfitdist' tool. In addition, we  
412 show the 95% confidence bounds of the GEV distribution and fit a non-parametric Weibull  
413 distribution to the data for comparison purposes. Hereinafter, we will use the GEV distribution to  
414 estimate WLs for 10, 50, 100, 200, 500, and 1000-year return periods.

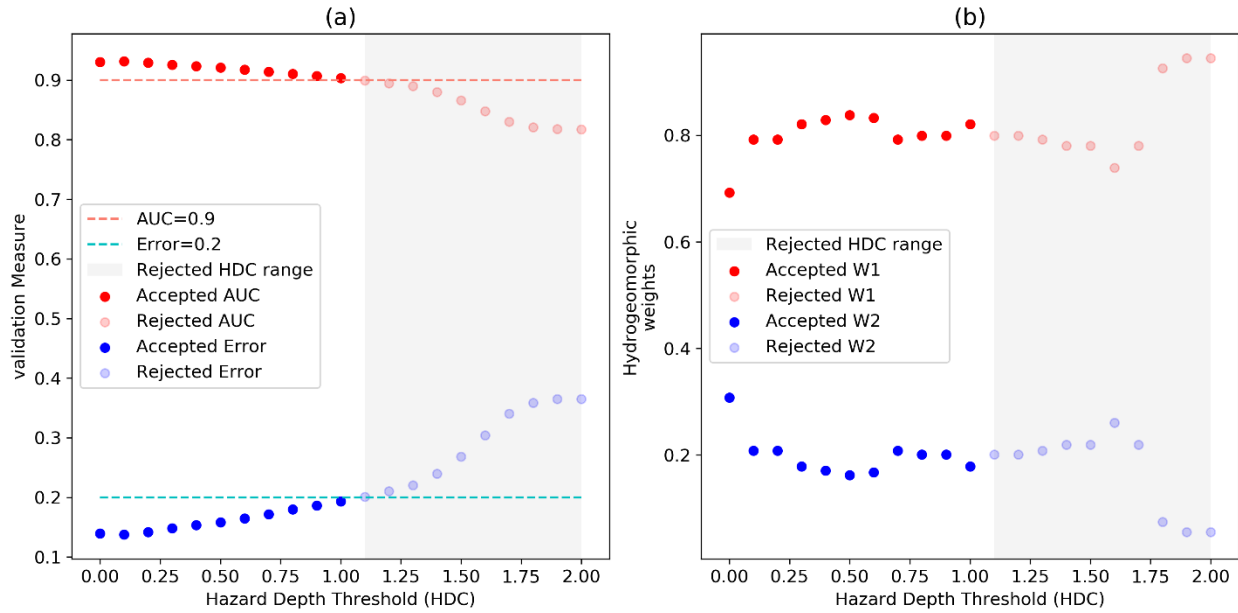


415

416 **Figure 5.** Return water levels (WLs) for Fort Pulaski station in Savannah GA (NOAA - 8670870).  
417 Plotting positions (black crosses) are derived from the Weibull formula based on annual block  
418 maxima time series (AMAX) and comparable to the Generalized Extreme Value (GEV)  
419 distribution (blue circles). 95% confidence intervals (CI) for the distribution parameters of the  
420 GEV distribution are shown with a shaded blue band.

421

422 After calibrating the Delft3D-FM model, we generate daily flood inundation maps for Hurricane  
423 Matthew, determine the maximum flood extent among all days, and then use an HDC to convert  
424 the maximum inundation map to a binary map of low and high hazard classes. Using 21 different  
425 HDCs ranging from 0 to 2 m, we perform 21 calibrations corresponding to a given reference flood  
426 hazard map generated from a specific HDC value. Figure 6a shows the *error* and AUC of  
427 calibration corresponding to different HDC values. As can be seen, increasing the HDC decreases  
428 the accuracy of the hydrogeomorphic method for flood hazard mapping. Looking into the errors  
429 and AUC values reported in the literature of binary flood hazard mapping studies, we consider an  
430 error of 0.2 and an AUC of 0.9 (dash lines) as the limits for distinguishing acceptable models from  
431 unacceptable ones. The grey region indicates the rejected HDC values above 1.1 m that result in  
432 unacceptable accuracy (e.g.,  $Error > 0.2$  or  $AUC < 0.9$ ). Figure 6b indicates the optimum weights  
433 calculated from the calibration of the hydrogeomorphic method corresponding to different HDC  
434 values. The higher value of  $w_1$  compared to  $w_2$  demonstrates that feature  $H$  is a more important  
435 factor than feature  $D$  in representing the flood hazard areas, and a combination of both features is  
436 the best indicator of floodplains compared to using each feature individually ( $w_1 = 0$  or  $w_2 = 0$ ).  
437 Figure 6b also shows that for the  $HDC = 0$  (wet vs dry classification), feature  $D$  shows the highest  
438 contribution (30%) while using the high HDC value of 2 m decreases the contribution of this  
439 feature to almost zero.

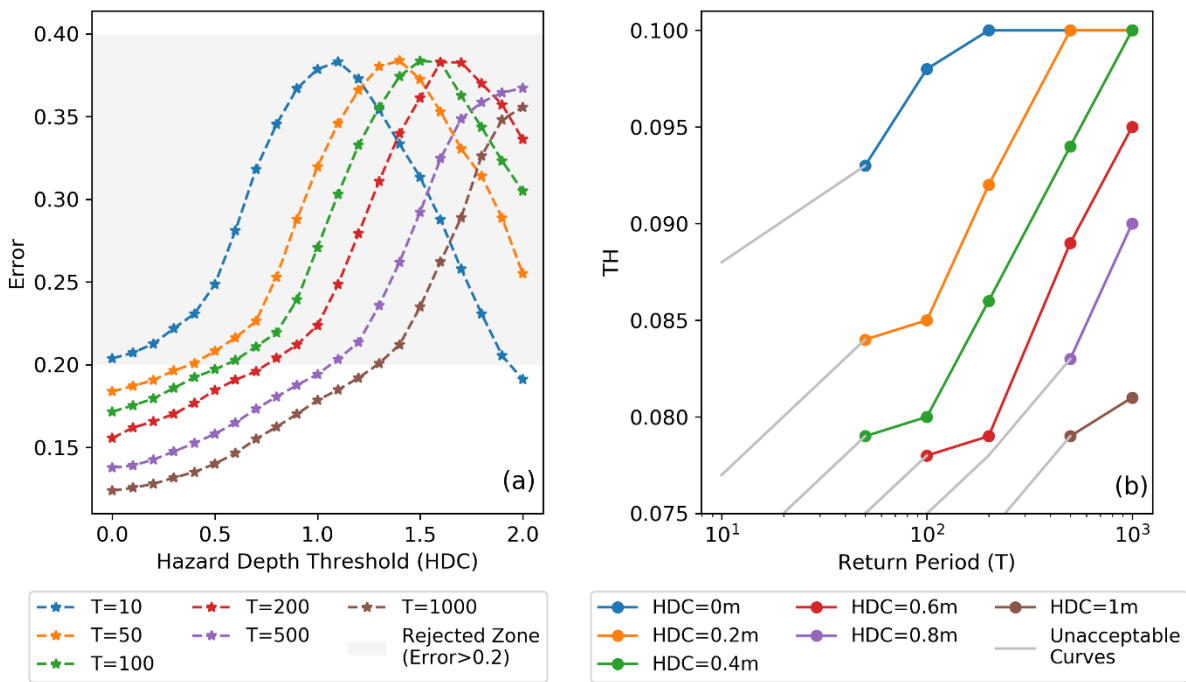


440

441 **Figure 6.** Calibration of  $I_{HD}$ -Hydrogeomorphic index for Hurricane Matthew. (a) the variation of  
 442 performance measures AUC (red) and error (blue) for different hazard depth cutoff (HDC) values  
 443 and (b) the optimum weights of the  $I_{HD}$ -hydrogeomorphic index for different HDC values. The  
 444 dash lines show the maximum error (0.2) and minimum AUC (0.9) that are acceptable for flood  
 445 hazard mapping. Using these criteria, the gray regions show that the hydrogeomorphic model  
 446 cannot provide acceptable results for HDC values higher than 1.1 m.

447 To generate the operative curves for future flood events, we design 36 scenarios that include 6-six  
 448 HDCs (0, 0.2, 0.4, 0.6, 0.8, 1 m) from the acceptable range of 0-1 m for six different reference  
 449 hazard maps, provided by the Delft3D-FM model for return periods of 10, 50, 100, 200, 500, and  
 450 1000 years. Each scenario provides a reference hazard map, so a binary classification is performed  
 451 to estimate TH corresponding to each scenario. Figure 7a indicates the error curves for different  
 452 return period events. For low HDCs, increasing the magnitude of the flood (higher return period)  
 453 results in more accuracy of the hydrogeomorphic method. This pattern is opposite for high HDCs  
 454 where flood event with a 10 year return period provides the highest accuracy. In general, the grey

455 region shows that for high HDCs, the performance of the hydrogeomorphic method is poor for  
 456 almost all return periods while for low HDCs, all flood events can be accurately used for flood  
 457 hazard mapping. Figure 7b illustrates the hydrogeomorphic threshold operative curves for future  
 458 flood hazard mapping. The  $TH$  in the y-axis is the key value that can be estimated for each  
 459 combination of HDC and return period. Knowing this threshold, Eq. 2 can be used to rapidly  
 460 estimate the hazard areas for future floods. As expected, a higher magnitude of flood needs a higher  
 461 hydrogeomorphic threshold while increasing HDC (smaller high-hazard areas) requires a smaller  
 462 threshold for binary classification. The grey parts of the curves refer to those scenarios that have  
 463 unacceptable accuracy so it is recommended to not use HDCs corresponding to these parts.

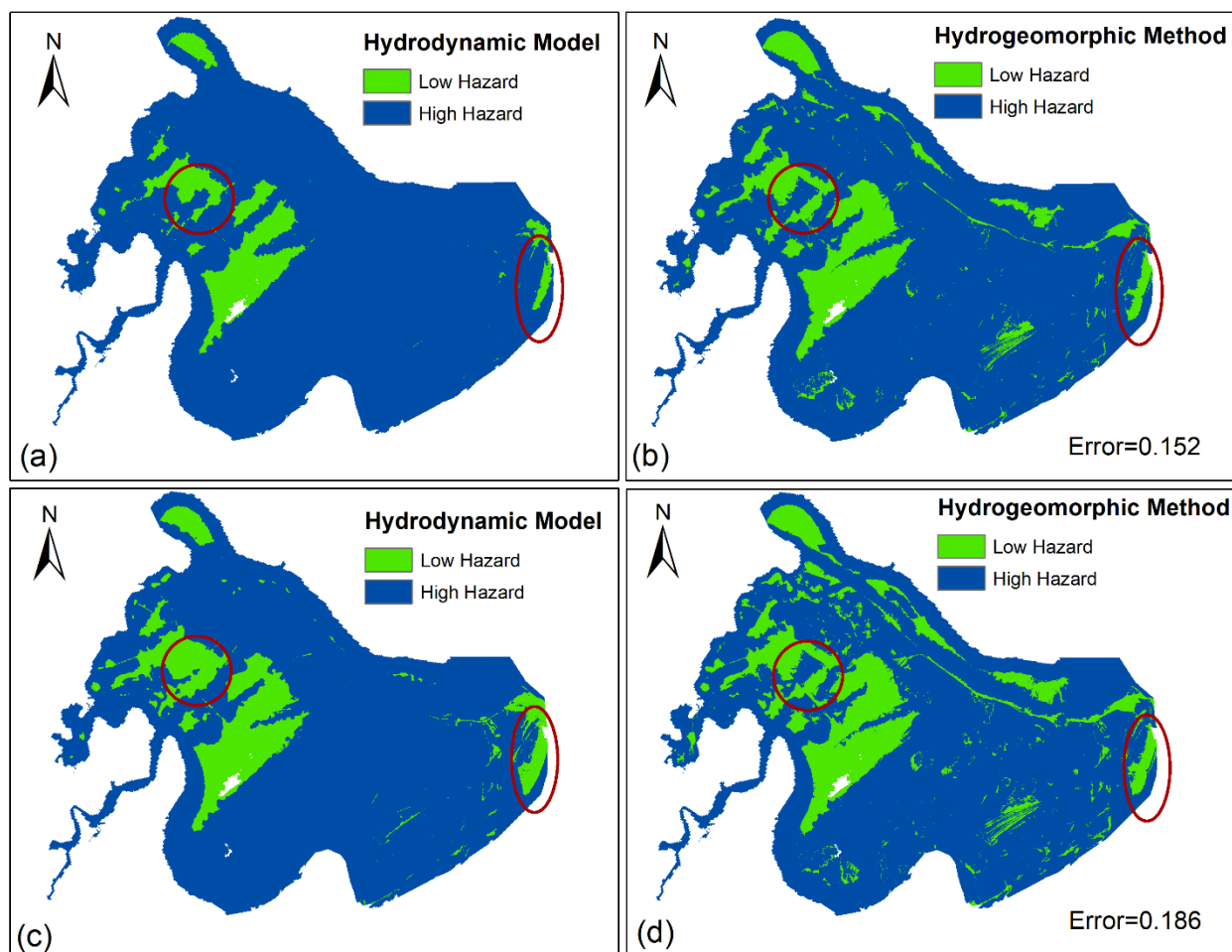


464  
 465 **Figure 7.** (a) The errors of flood hazard maps generated by the calibrated hydrogeomorphic  
 466 method for different return period flood events and hazard depth cutoff (HDC) values. (b) The  
 467 hydrogeomorphic threshold operative curves provided for different HDC values. These operative

468 curves are the major tool for fast flood hazard mapping as depending on the return period of a  
469 future flood event and the HDC value chosen by the decision-maker, the operative curves estimate  
470 the hydrogeomorphic threshold. Knowing this threshold, the flood hazard map will be generated  
471 in a few minutes.

472 Finally, we evaluate the accuracy and effectiveness of the proposed operative curves by validating  
473 their performance in generating flood hazard areas during Hurricane Irma. The maximum WL  
474 during this flood event was 2.49 m ~~that~~ which corresponds to a 223-year flood event according to  
475 our flood frequency analysis (e.g., GEV distribution). For two HDCs of 0 and 0.6 m, the operative  
476 curves suggest the hydrogeomorphic thresholds of 0.1 and 0.08, respectively. Using these  
477 thresholds and Eq.2, the flood hazard maps corresponding to Hurricane Irma can be generated.  
478 Figure 8 indicates a side by side comparison of flood hazard maps generated by the Delft3D-FM  
479 model (Figures 8a and 8c) and the hydrogeomorphic threshold operative curves (Figures 8b and  
480 8d) for two different HDCs of 0 (Figures 8a and 8b) and 0.6 m (Figures 8c and 8d). For both HDCs,  
481 errors (0.152 and 0.186) are less than a 0.2 limit used for reliable flood hazard mapping. The main  
482 ~~errors of the hydrogeomorphic method~~ discrepancies are some noisy scattered low-hazard areas  
483 located in the east and southeast of the study area. These areas can reflect the flooded surface  
484 depressions (sinks) resulting from the pluvial impacts of extreme precipitation. Hydrodynamic  
485 models simulate the fluvial and coastal processes that occur adjacent to rivers and oceans while  
486 disregarding the pluvial impacts. The red circle in the left part of the figures ~~also~~ shows a region  
487 that the hydrogeomorphic method cannot properly simulate, especially for higher HDCs. This can  
488 be due to the inability of the hydrogeomorphic method to properly simulate physical processes.  
489 On the other hand, the red eclipse at the right side of the figures illustrates an urbanized region  
490 where the hydrogeomorphic method properly classifies the area compared to the reference map.

491 Overall, the high overlap of the flood hazard maps provided by the hydrogeomorphic method with  
492 the reference maps provided by the hydrodynamic model (error <math><0.2</math>) illustrates the reliability and  
493 effectiveness of the proposed hydrogeomorphic method for flood hazard mapping. Besides, the  
494 high efficiency of this approach for rapid estimation of flood hazard maps (order of minutes)  
495 compared to the long computational time required for detailed hydrodynamic modeling (order of  
496 hours) suggests the proposed hydrogeomorphic method as an alternative for efficient flood hazard  
497 mapping during emergencies.



498  
499 **Figure 8.** Validation results for Hurricane Irma showing a side-by-side comparison of flood  
500 hazard maps generated by the hydrodynamic model and hydrogeomorphic method for two

501 different hazard depth cutoffs (HDCs), HDC=0 (a, b) and HDC=0.6 m (c, d). To generate the  
502 flood hazard maps by the hydrogeomorphic method, the operative curves estimate two  
503 hydrogeomorphic thresholds of 0.1 and 0.08 for HDC= 0 m and HDC= 0.6 m, respectively while  
504 the return period of Hurricane Irma is estimated as a 223 years flood event.

## 505 **5. Discussion**

506 This study develops hydrogeomorphic threshold operative curves for rapid estimation of hazardous  
507 areas during emergencies of future coastal floods in deltas and estuaries. The low errors (<0.2) of  
508 estimated hazard maps for Hurricane Irma generated by the proposed approach compared to the  
509 reference hydrodynamic model results demonstrate the high accuracy of the proposed operative  
510 curves for future flood events in this region. According to studies conducted on the binary  
511 classification of hydrogeomorphic features in the literature, the errors of the best classifiers were  
512 mostly in the range of 0.2-0.3 for inland floods (Degiorgis et al., 2012; Manfreda et al., 2014).  
513 Therefore, given the more complexity of terrain and drainage network in deltas, predicting the  
514 hazard maps with errors less than 0.2 (e.g. error of 0.152 for HDC=0) is a promising achievement.  
515 The potential reasons explaining a high accuracy of the proposed binary classifier for wetlands  
516 include the high-resolution DEM used for mapping (~3m); and the incorporation of bathymetry  
517 into DEM. In addition, the flexible structure of the proposed hydrogeomorphic index, with two  
518 varying weights of  $H$  and  $D$  features, allows for calibrating the index with the optimum  
519 contribution of each feature, which in return results in the highest accuracy.

520 The proposed hydrogeomorphic index ( $I_{HD}$ ) is the primary data for flood hazard mapping in this  
521 study. Thus, the quality of two main inputs of this index, namely the DEM and stream network  
522 used to calculate features  $H$  and  $D$  play a vital role in the overall accuracy of the proposed  
523 approach. To obtain maximum accuracy, here we used the best available DEM with the finest

524 spatial resolution of 3 m that includes the bathymetry data. However, considering the limited  
525 access to such high-quality DEMs in many areas of the world, it is recommended to evaluate the  
526 sensitivity of the proposed approach to lower quality DEMs (e.g. 30 m and 90 m DEMs without  
527 bathymetry information) in future studies. Another piece of research can investigate the sensitivity  
528 of the proposed approach to the density of the drainage network used for calculating the  $I_{HD}$  index.

529 Unlike past studies that used binary classifiers for detecting hazard areas corresponding to past  
530 floods or generated static maps for a specific return period ~~event~~ (Degiorgis et al., 2012;  
531 Jafarzadegan et al., 2018; Manfreda et al., 2015b; Samela et al., 2017), here we propose the  
532 hydrogeomorphic threshold operative curves for real-time flood hazard mapping. Considering the  
533 rapid occurrence of hurricane-induced flooding in deltas and estuaries, these curves can be highly  
534 beneficial for emergency responders to provide a preliminary estimation of hazard areas for an  
535 upcoming flood in these regions and design the appropriate evacuation strategies. In addition, the  
536 proposed operative curves demonstrate the hydrogeomorphic threshold variations with HDCs.  
537 This feature of the operative curves gives additional flexibility to decision-makers for estimating  
538 the hazard maps based on the HDC that is considered given the momentary safety issues. For  
539 example, identifying the hazard map based on  $HDC < 0.3$  is useful for checking the operability and  
540 accessibility of essential facilities and infrastructure, while a hazard map corresponding to  $HDC = 1$   
541 indicates those areas that experience high WLs above 1 m as hazardous areas, with greater potential  
542 for casualties and significant structural damage. Overall, the hydrogeomorphic threshold operative  
543 curves are a function of both the return period (flood severity) and HDC (a decision-making option  
544 that controls the definition of high hazard). Using a similar approach, future studies can provide  
545 these curves for inland floods as well. In addition, due to the practical benefits of these curves for  
546 efficient coastal flood hazard assessment, the hydrogeomorphic threshold operative curves can be

547 extended to other deltas and estuaries that experience frequent flooding across the US (e.g.,  
548 Mississippi -- [Louisiana \(LA\)](#), Galveston Bay -- [Texas \(TX\)](#), Delaware Bay -- [Delaware \(DE\)](#),  
549 Chesapeake Bay -- [Virginia \(VA\)](#), among others) and the world (e.g. Yangtze - China,  
550 Brahmaputra - Bangladesh, among others). To implement this approach, first, a hydrodynamic  
551 model should be set up for the new study area and generate reference inundation maps for different  
552 return periods. Access to observed water level data (gauges or HWMs) and flood extent maps from  
553 past floods is required to properly calibrate the hydrodynamic model. Then the  $I_{HD}$  index  
554 calculated from a DEM is utilized together with the reference maps to provide the  
555 hydrogeomorphic threshold operative curves for future floods.

556 The reference maps used for training the binary classifier are key components for generating  
557 reliable results. Since these reference maps are the outcomes of hydrodynamic modeling, they are  
558 prone to uncertainties stemming from unrealistic parametrization, imperfect model structure, and  
559 erroneous forcing. The design floods used as boundary conditions of the hydrodynamic model are  
560 estimated from flood frequency analysis that is prone to uncertainty as well. Here, we used a  
561 bivariate approach that estimates the design flood based on the water level data. A more  
562 comprehensive flood frequency analysis that accounts for other flood attributes, such as volume,  
563 spatial dependencies, or nonstationarity--can improve the reliability of flood frequency analysis in  
564 future studies (Brunner et al., 2016; Yan and Moradkhani, 2015; Bracken et al., 2018).  
565 to less than 100 years of data for flood frequency analysis, the extreme return levels (i.e. ~~500~~  
566 ~~year~~500- and 1000-year floods) pose high uncertainties due to the extrapolation of annual  
567 maxima data. This should warn decision-makers to be more cautious about using operative curves  
568 for extreme flood events. For future studies, the uncertainty bounds of flood frequency analysis  
569 (especially extrapolations for extreme cases) can be considered in the modeling. In a real-time

570 scenario, the forecasted WL used for flood frequency analysis is also prone to uncertainties  
571 originating from imperfect forecasting methods and nonstationary climate data. In addition, the  
572 uncertainty of model parametrization can be accounted for by running the hydrodynamic model  
573 for different combinations of optimum parameters. Model structure uncertainty can be also  
574 considered by using different hydrodynamic models and combining the results. Finally,  
575 probabilistic reference maps together with uncertainties involved in WL forecasting and flood  
576 frequency analysis can be integrated to develop probabilistic hydrogeomorphic threshold operative  
577 curves in future studies. This is in line with the report provided for the NOAA National Weather  
578 Service (NWS), showing the NWS stakeholder's preference for utilizing probabilistic storm surge  
579 inundation maps ~~in the future~~ (Eastern Research Group, Inc, 2013).

580 Operationally, The probabilistic operative curves account for the major source of uncertainties and  
581 provide a more reliable decision-making tool for coastal flood hazard mapping.  
582 ~~The operative hydrogeomorphic threshold classifiers proposed for real-time coastal flood hazard~~  
583 ~~mapping can be used as an alternative tool for the rapid estimation of hazardous areas. In the~~  
584 ~~operational mode, the water level forecasts provided by the NWS can be used to estimate the return~~  
585 ~~period of an upcoming coastal flood event.~~ the Sea, Lake, and Overland Surges from Hurricanes  
586 (SLOSH) model (Jelesnianski et al., 1984) is the storm surge model currently used by NWS to  
587 perform storm surge forecasting and create probabilistic flood inundation maps for real-time  
588 tropical storms (Sea, Lake, and Overland Surges from Hurricanes (SLOSH), 2022). The feature of  
589 SLOSH that makes it the preferred model of the NWS for storm surge forecasting and mapping is  
590 the model's computational efficiency that allows the model to be run as an ensemble (Forbes et  
591 al., 2014). However, SLOSH is just one of several modeling options for storm surge modeling and  
592 mapping, each possessing strengths and weaknesses associated with their simulations. The

593 inclusion of additional models that can create flood maps of storm surges for a given event should  
594 provide an enhanced understanding of the uncertainty of inundation at a given location (Teng et  
595 al., 2015). However, the higher computational burden of alternative models, such as Delft3D-FM,  
596 tend to preclude their use in real-time operations and certainly, their use in generating an ensemble  
597 necessary for probabilistic flood maps. The methodology we propose in this manuscript may offer  
598 the NWS and other agencies a means to utilize alternatives to SLOSH for flood inundation  
599 mapping and probabilistic flood inundation mapping on U.S. coastlines. Models such as Delft3D-  
600 FM can generate reference maps to train the binary classifier and build the probabilistic operating  
601 curves. Using the proposed operative curves, the hydrogeomorphic threshold is determined and t  
602 The probabilistic operative curves would account for the major source of uncertainties and provide  
603 a computationally efficient and reliable decision-making tool for coastal planners and floodplain  
604 managers. The operative hydrogeomorphic threshold classifiers proposed for real-time coastal  
605 flood hazard mapping can be used as an alternative tool for the rapid estimation of hazardous areas  
606 during real-time flood events. In an operational mode, water level or meteorological forecasts can  
607 be used to estimate the return period of an upcoming coastal flood event and the methodology here  
608 can utilize this as an input to perform LCFM flood inundation mapping both deterministically and  
609 probabilistically.

610 ~~he flood hazard map is generated. The Sea, Lake, and Overland Surges from Hurricanes (SLOSH)~~  
611 ~~model is an LCFM tool currently used by NWS to estimate probabilistic storm surge forecasts.~~  
612 ~~The flood inundation maps generated by this model are the results of overlaying storm surge~~  
613 ~~forecast with DEM. The model doesn't consider the streamflow network and riverine flood~~  
614 ~~mechanisms. On the other hand, our proposed hydrogeomorphic index uses both streamflow~~  
615 ~~network and DEM to provide a more detailed representation of the flooding in coastal areas.~~

616 Another LCFM approach is to train machine learning algorithms on reference inundation maps  
617 provided by well-calibrated hydrodynamic models (Bass and Bedient, 2018). A benchmark study  
618 that compares the performance (accuracy and efficiency) of ~~three-two~~ LCFM methods, including  
619 our proposed DEM-based hydrogeomorphic classifier, and the surrogate machine learning-based  
620 algorithm, and the SLOSH model is highly recommended for future studies.

~~621 The probabilistic operative curves account for the major source of uncertainties and provide a more~~  
~~622 reliable decision making tool for coastal flood hazard mapping. The operative hydrogeomorphic~~  
~~623 threshold classifiers proposed for real-time coastal flood hazard mapping can be used as an~~  
~~624 alternative tool for the rapid estimation of hazardous areas. In the operational mode, the water level~~  
~~625 forecasts provided by the NWS can be used to estimate the return period of an upcoming coastal~~  
~~626 flood event.~~

## 627 **6. Summary and Conclusions**

628 In this study, we proposed binary classifiers for efficient flood hazard mapping in deltas and  
629 estuaries. The HAND, typically used for modeling inland ~~flooding~~floods, is modified for flat  
630 regions along the coastline, and a new hydrogeomorphic index ( $I_{HD}$ ) that comprises both HAND  
631 and distance to nearest drainage was developed. The DEM used as the base of these binary  
632 classifiers is a 3 m Lidar that includes bathymetric information. This is another improvement  
633 compared to previous DEM-based classifiers that commonly used 10-30 m DEMs without  
634 bathymetric data. The  $I_{HD}$  index has two unknown weights that show the contribution of both  
635 HAND and feature  $D$ . We simulated Hurricane Matthew with the Delft3D-FM model and used the  
636 results as a reference flood hazard map to calibrate the  $I_{HD}$  index. Using Delft3D-FM again, we  
637 generated six flood hazard maps corresponding to different return periods and employed these  
638 maps as a reference to generate the hydrogeomorphic threshold operative curves. Finally, we

639 validated the proposed operative curves for reliable and efficient flood hazard mapping by  
640 comparing the flood hazard maps generated for Hurricane Irma with the proposed curves and the  
641 Delft3D-FM model. The high accuracy of validation results (<0.2 error) together with the ~~rapid~~  
642 fast computational efficiency of this approach for real-time flood hazard mapping suggests the  
643 proposed operative curves as a practical decision-making tool for on-time and reliable estimation  
644 of hazard areas in estuaries.

645

## 646 **Data availability**

647 All the data used in this study, including the gauge streamflow and water stage data are publicly  
648 available from the USGS and NOAA websites. The High Water Marks provided for Hurricanes  
649 Irma and Matthew are available from the USGS Flood Event Viewer platform.

## 650 **Author contribution**

651 KJafarzadegan and HMoradkhani conceptualized the study. KJafarzadegan designed the whole  
652 framework and implemented the hydrogeomorphic methodology. DMuñoz implemented the  
653 hydrodynamic modeling. KJafarzadegan and DMuñoz wrote the first draft of the manuscript.  
654 HMoradkhani, HMoftakhari, JGutenson, and GSavant provided comments and edited the  
655 manuscript.

## 656 **Competing interests**

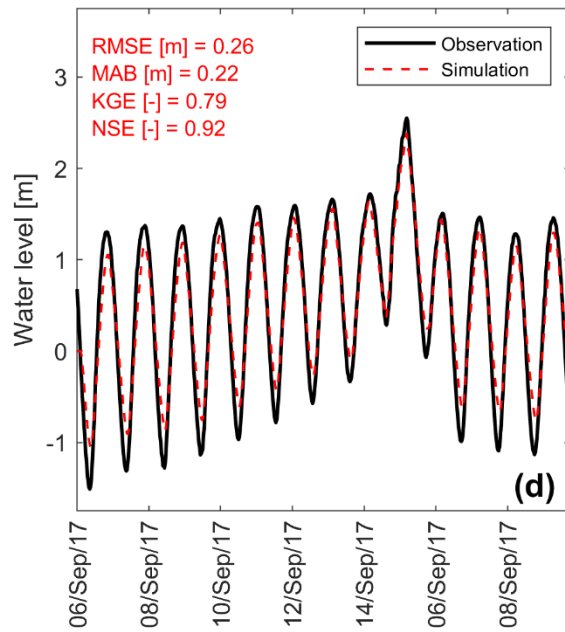
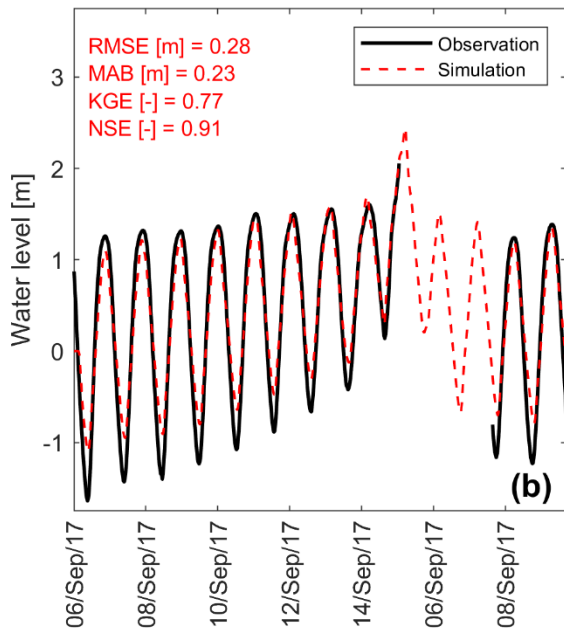
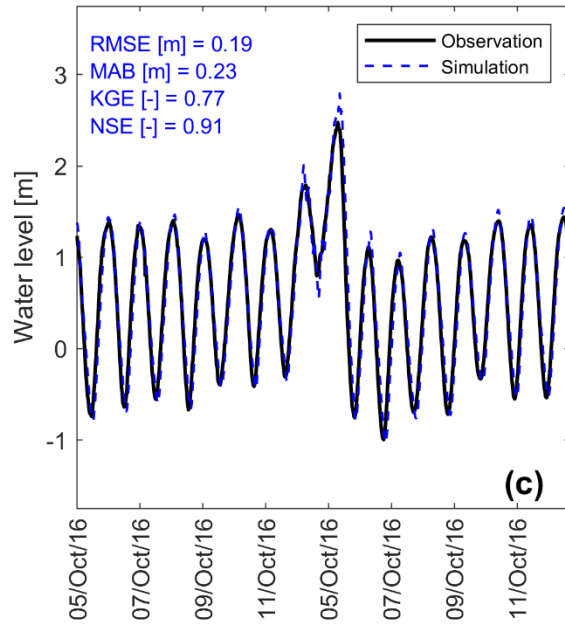
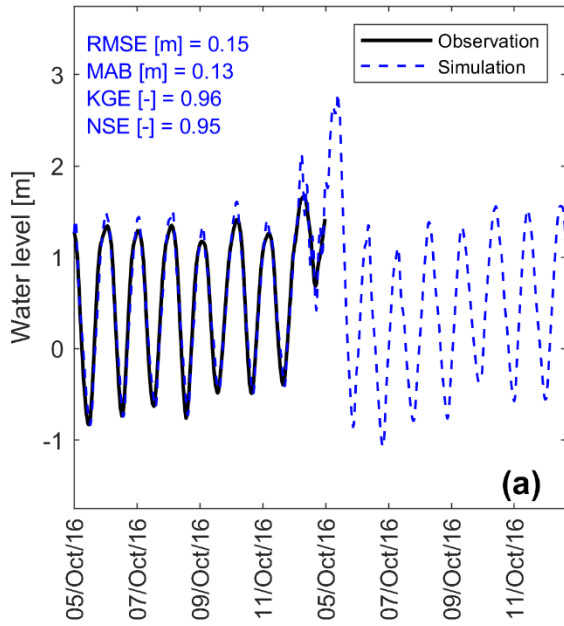
657 The authors declare that they have no conflict of interest.

658

659 **Acknowledgment**

660 This work was financially supported by the USACE award # A20-0545-001. We would like to  
661 thank the anonymous reviewers for their constructive comments on the original version of the  
662 manuscript.

663 **Supplementary Material**



664

665

666

667

**Figure S1.** Calibration and validation of the Savannah Delft3D-FM model. Time series of simulated and observed WLS at (a, b) Port Wentworth and (c, d) Savannah River at USACE dock. Top and bottom panel show times series of Hurricane Matthew and Irma, respectively. Note that

668 [the model can simulate water level variability, and so fill the data gaps observed during the](#)  
669 [Hurricanes.](#)

## 670 **References**

- 671 Afshari, S., Tavakoly, A. A., Rajib, M. A., Zheng, X., Follum, M. L., Omranian, E., and Fekete, B. M.:  
672 Comparison of new generation low-complexity flood inundation mapping tools with a hydrodynamic  
673 model, *J. Hydrol.*, 556, 539–556, <https://doi.org/10.1016/j.jhydrol.2017.11.036>, 2018.
- 674 Alizad, K., Hagen, S. C., Medeiros, S. C., Bilskie, M. V., Morris, J. T., Balthis, L., and Buckel, C. A.: Dynamic  
675 responses and implications to coastal wetlands and the surrounding regions under sea level rise, *PLOS*  
676 *ONE*, 13, e0205176, <https://doi.org/10.1371/journal.pone.0205176>, 2018.
- 677 Sea, Lake, and Overland Surges from Hurricanes (SLOSH): <https://www.nhc.noaa.gov/surge/slosh.php>,  
678 last access: 18 January 2022.
- 679 USGS Surface Water Information: <https://water.usgs.gov/osw/iwrss/>, last access: 16 November 2021.
- 680 Arcement, G. J. and Schneider, V. R.: Guide for selecting Manning's roughness coefficients for natural  
681 channels and flood plains, 1989.
- 682 Barbier, E. B.: Chapter 27 - The Value of Coastal Wetland Ecosystem Services, in: *Coastal Wetlands*,  
683 edited by: Perillo, G. M. E., Wolanski, E., Cahoon, D. R., and Hopkinson, C. S., Elsevier, 947–964,  
684 <https://doi.org/10.1016/B978-0-444-63893-9.00027-7>, 2019.
- 685 Bass, B. and Bedient, P.: Surrogate modeling of joint flood risk across coastal watersheds, *J. Hydrol.*, 558,  
686 159–173, <https://doi.org/10.1016/j.jhydrol.2018.01.014>, 2018.
- 687 Bates, P. D., Horritt, M. S., and Fewtrell, T. J.: A simple inertial formulation of the shallow water  
688 equations for efficient two-dimensional flood inundation modelling, *J. Hydrol.*, 387, 33–45,  
689 <https://doi.org/10.1016/j.jhydrol.2010.03.027>, 2010.
- 690 Bates, P. D., Quinn, N., Sampson, C., Smith, A., Wing, O., Sosa, J., Savage, J., Olcese, G., Neal, J.,  
691 Schumann, G., Giustarini, L., Coxon, G., Porter, J. R., Amodeo, M. F., Chu, Z., Lewis-Gruss, S., Freeman, N.  
692 B., Houser, T., Delgado, M., Hamidi, A., Bolliger, I., E. McCusker, K., Emanuel, K., Ferreira, C. M., Khalid,  
693 A., Haigh, I. D., Couasnon, A., E. Kopp, R., Hsiang, S., and Krajewski, W. F.: Combined Modeling of US  
694 Fluvial, Pluvial, and Coastal Flood Hazard Under Current and Future Climates, *Water Resour. Res.*, 57,  
695 e2020WR028673, <https://doi.org/10.1029/2020WR028673>, 2021.
- 696 Bracken, C., Holman, K. D., Rajagopalan, B., and Moradkhani, H.: A Bayesian hierarchical approach to  
697 multivariate nonstationary hydrologic frequency analysis, *Water Resour. Res.*, 54, 243–255, 2018.
- 698 Brunner, M. I., Seibert, J., and Favre, A.-C.: Bivariate return periods and their importance for flood peak  
699 and volume estimation, *WIREs Water*, 3, 819–833, <https://doi.org/10.1002/wat2.1173>, 2016.

700 Carlston, C. W.: Longitudinal Slope Characteristics of Rivers of the Midcontinent and the Atlantic East  
701 Gulf Slopes, *Int. Assoc. Sci. Hydrol. Bull.*, 14, 21–31, <https://doi.org/10.1080/02626666909493751>, 1969.

702 Chow Ven, T.: *Open channel hydraulics*, 1959.

703 Davidson, N. C.: How much wetland has the world lost? Long-term and recent trends in global wetland  
704 area, *Mar. Freshw. Res.*, 65, 934–941, <https://doi.org/10.1071/MF14173>, 2014.

705 Degiorgis, M., Gnecco, G., Gorni, S., Roth, G., Sanguineti, M., and Taramasso, A. C.: Classifiers for the  
706 detection of flood-prone areas using remote sensed elevation data, *J. Hydrol.*, 470–471, 302–315,  
707 <https://doi.org/10.1016/j.jhydrol.2012.09.006>, 2012.

708 Degiorgis, M., Gnecco, G., Gorni, S., Roth, G., Sanguineti, M., and Taramasso, A. C.: Flood Hazard  
709 Assessment Via Threshold Binary Classifiers: Case Study of the Tanaro River Basin, *Irrig. Drain.*, 62, 1–10,  
710 <https://doi.org/10.1002/ird.1806>, 2013.

711 Delft3D Flexible Mesh Suite - Deltares: [https://www.deltares.nl/en/software/delft3d-flexible-mesh-](https://www.deltares.nl/en/software/delft3d-flexible-mesh-suite/)  
712 [suite/](https://www.deltares.nl/en/software/delft3d-flexible-mesh-suite/), last access: 15 November 2021.

713 Dodov, B. A. and Foufoula-Georgiou, E.: Floodplain morphometry extraction from a high-resolution  
714 digital elevation model: a simple algorithm for regional analysis studies, *IEEE Geosci. Remote Sens. Lett.*,  
715 3, 410–413, <https://doi.org/10.1109/LGRS.2006.874161>, 2006.

716 Eastern Research Group, Inc: Hurricane Forecast Improvement Program Socio-Economic Research and  
717 Recommendations:, NOAA National Weather Service, 2013.

718 Fagherazzi, S., Mariotti, G., Banks, A. T., Morgan, E. J., and Fulweiler, R. W.: The relationships among  
719 hydrodynamics, sediment distribution, and chlorophyll in a mesotidal estuary, *Estuar. Coast. Shelf Sci.*,  
720 144, 54–64, <https://doi.org/10.1016/j.ecss.2014.04.003>, 2014.

721 Familkhalili, R., Talke, S. A., and Jay, D. A.: Tide-Storm Surge Interactions in Highly Altered Estuaries: How  
722 Channel Deepening Increases Surge Vulnerability, *J. Geophys. Res. Oceans*, 125, e2019JC015286,  
723 <https://doi.org/10.1029/2019JC015286>, 2020.

724 Fawcett, T.: An introduction to ROC analysis, *Pattern Recognit. Lett.*, 27, 861–874,  
725 <https://doi.org/10.1016/j.patrec.2005.10.010>, 2006.

726 Forbes, C., Rhome, J., Mattocks, C., and Taylor, A.: Predicting the Storm Surge Threat of Hurricane Sandy  
727 with the National Weather Service SLOSH Model, *J. Mar. Sci. Eng.*, 2, 437–476,  
728 <https://doi.org/10.3390/jmse2020437>, 2014.

729 Ghanbari, M., Arabi, M., Kao, S.-C., Obeysekera, J., and Sweet, W.: Climate Change and Changes in  
730 Compound Coastal-Riverine Flooding Hazard Along the U.S. Coasts, *Earths Future*, 9, e2021EF002055,  
731 <https://doi.org/10.1029/2021EF002055>, 2021.

732 Gharari, S., Hrachowitz, M., Fenicia, F., and Savenije, H. H. G.: Hydrological landscape classification:  
733 investigating the performance of HAND based landscape classifications in a central European meso-scale  
734 catchment, *Hydrol. Earth Syst. Sci.*, 15, 3275–3291, <https://doi.org/10.5194/hess-15-3275-2011>, 2011.

735 Gutenson, J.: A Review of Current and Future NWS Services, 2020.

736 Gutenson, J. L., Tavakoly, A. A., Massey, T. C., Savant, G., Tritinger, A. S., Owensby, M. B., Wahl, M. D.,  
737 and Islam, M. S.: Investigating Modeling Strategies to Couple Inland Hydrology and Coastal Hydraulics to  
738 Better Understand Compound Flood Risk, 64–75, <https://doi.org/10.1061/9780784483466.006>, 2021.

739 Helton, J. C. and Davis, F. J.: Latin hypercube sampling and the propagation of uncertainty in analyses of  
740 complex systems, *Reliab. Eng. Syst. Saf.*, 81, 23–69, 2003.

741 IWRSS: Requirements for the National Flood Inundation Mapping Services, National Oceanic and  
742 Atmospheric Administration United States Army Corps of Engineers United States Geological Survey,  
743 2013.

744 IWRSS: Design for the National Flood Inundation Mapping Services, National Oceanic and Atmospheric  
745 Administration United States Army Corps of Engineers United States Geological Survey, 2015.

746 Jafarzadegan, K. and Merwade, V.: A DEM-based approach for large-scale floodplain mapping in  
747 ungauged watersheds, *J. Hydrol.*, 550, 650–662, <https://doi.org/10.1016/j.jhydrol.2017.04.053>, 2017.

748 Jafarzadegan, K. and Merwade, V.: Probabilistic floodplain mapping using HAND-based statistical  
749 approach, *Geomorphology*, 324, 48–61, <https://doi.org/10.1016/j.geomorph.2018.09.024>, 2019.

750 Jafarzadegan, K., Merwade, V., and Saksena, S.: A geomorphic approach to 100-year floodplain mapping  
751 for the Conterminous United States, *J. Hydrol.*, 561, 43–58,  
752 <https://doi.org/10.1016/j.jhydrol.2018.03.061>, 2018.

753 Jafarzadegan, K., Merwade, V., and Moradkhani, H.: Combining clustering and classification for the  
754 regionalization of environmental model parameters: Application to floodplain mapping in data-scarce  
755 regions, *Environ. Model. Softw.*, 125, 104613, <https://doi.org/10.1016/j.envsoft.2019.104613>, 2020.

756 Jafarzadegan, K., Abbaszadeh, P., and Moradkhani, H.: Sequential Data Assimilation for Real-Time  
757 Probabilistic Flood Inundation Mapping, *Hydrol. Earth Syst. Sci. Discuss.*, 1–39,  
758 <https://doi.org/10.5194/hess-2021-181>, 2021.

759 Jelesnianski, C., Chen, J., Shaffer, W., and Gilad, A.: SLOSH - A Hurricane Storm Surge Forecast Model, in:  
760 *OCEANS 1984*, *OCEANS 1984*, 314–317, <https://doi.org/10.1109/OCEANS.1984.1152341>, 1984.

761 Khojasteh, D., Chen, S., Felder, S., Heimhuber, V., and Glamore, W.: Estuarine tidal range dynamics  
762 under rising sea levels, *PLOS ONE*, 16, e0257538, <https://doi.org/10.1371/journal.pone.0257538>, 2021a.

763 Khojasteh, D., Glamore, W., Heimhuber, V., and Felder, S.: Sea level rise impacts on estuarine dynamics:  
764 A review, *Sci. Total Environ.*, 780, 146470, <https://doi.org/10.1016/j.scitotenv.2021.146470>, 2021b.

765 Kirwan, M. L. and Megonigal, J. P.: Tidal wetland stability in the face of human impacts and sea-level  
766 rise, *Nature*, 504, 53–60, <https://doi.org/10.1038/nature12856>, 2013.

767 Kulp, S. A. and Strauss, B. H.: New elevation data triple estimates of global vulnerability to sea-level rise  
768 and coastal flooding, *Nat. Commun.*, 10, 4844, <https://doi.org/10.1038/s41467-019-12808-z>, 2019.

769 Kumbier, K., Carvalho, R. C., Vafeidis, A. T., and Woodroffe, C. D.: Investigating compound flooding in an  
770 estuary using hydrodynamic modelling: a case study from the Shoalhaven River, Australia, *Nat. Hazards*  
771 *Earth Syst. Sci.*, 18, 463–477, <https://doi.org/10.5194/nhess-18-463-2018>, 2018.

772 Land, M., Tonderski, K., and Verhoeven, J. T. A.: Wetlands as Biogeochemical Hotspots Affecting Water  
773 Quality in Catchments, in: *Wetlands: Ecosystem Services, Restoration and Wise Use*, edited by: An, S.  
774 and Verhoeven, J. T. A., Springer International Publishing, Cham, 13–37, [https://doi.org/10.1007/978-3-030-14861-4\\_2](https://doi.org/10.1007/978-3-030-14861-4_2), 2019.

776 Liu, Z., Merwade, V., and Jafarzaghan, K.: Investigating the role of model structure and surface  
777 roughness in generating flood inundation extents using one- and two-dimensional hydraulic models, *J.*  
778 *Flood Risk Manag.*, 12, e12347, 2019.

779 Longenecker, H. E., Graeden, E., Kluskiewicz, D., Zuzak, C., Rozelle, J., and Aziz, A. L.: A rapid flood risk  
780 assessment method for response operations and nonsubject-matter-expert community planning, *J.*  
781 *Flood Risk Manag.*, 13, e12579, <https://doi.org/10.1111/jfr3.12579>, 2020.

782 Luettich, R. A. (Richard A.), Westerink, J. J., and Scheffner, N. W.: ADCIRC : an advanced three-  
783 dimensional circulation model for shelves, coasts, and estuaries. Report 1, Theory and methodology of  
784 ADCIRC-2DD1 and ADCIRC-3DL, *This Digit. Resour. Was Creat. Scans Print Resour.*, 1992.

785 Maidment, D. R.: Conceptual Framework for the National Flood Interoperability Experiment, *JAWRA J.*  
786 *Am. Water Resour. Assoc.*, 53, 245–257, <https://doi.org/10.1111/1752-1688.12474>, 2017.

787 Maidment, D. R., Clark, E., Hooper, R., and Ernest, A.: National Flood Interoperability Experiment, in:  
788 *AGU Fall Meeting Abstracts*, 2014.

789 Manfreda, S., Di Leo, M., and Sole, A.: Detection of Flood-Prone Areas Using Digital Elevation Models, *J.*  
790 *Hydrol. Eng.*, 16, 781–790, [https://doi.org/10.1061/\(ASCE\)HE.1943-5584.0000367](https://doi.org/10.1061/(ASCE)HE.1943-5584.0000367), 2011.

791 Manfreda, S., Nardi, F., Samela, C., Grimaldi, S., Taramasso, A. C., Roth, G., and Sole, A.: Investigation on  
792 the use of geomorphic approaches for the delineation of flood prone areas, *J. Hydrol.*, 517, 863–876,  
793 <https://doi.org/10.1016/j.jhydrol.2014.06.009>, 2014.

794 Manfreda, S., Samela, C., Gioia, A., Consoli, G. G., Iacobellis, V., Giuzio, L., Cantisani, A., and Sole, A.:  
795 Flood-prone areas assessment using linear binary classifiers based on flood maps obtained from 1D and  
796 2D hydraulic models, *Nat. Hazards*, 79, 735–754, <https://doi.org/10.1007/s11069-015-1869-5>, 2015a.

797 Manfreda, S., Samela, C., Gioia, A., Consoli, G. G., Iacobellis, V., Giuzio, L., Cantisani, A., and Sole, A.:  
798 Flood-prone areas assessment using linear binary classifiers based on flood maps obtained from 1D and  
799 2D hydraulic models, *Nat. Hazards*, 79, 735–754, <https://doi.org/10.1007/s11069-015-1869-5>, 2015b.

800 McGlynn, B. L. and McDonnell, J. J.: Quantifying the relative contributions of riparian and hillslope zones  
801 to catchment runoff, *Water Resour. Res.*, 39, <https://doi.org/10.1029/2003WR002091>, 2003.

802 McGlynn, B. L. and Seibert, J.: Distributed assessment of contributing area and riparian buffering along  
803 stream networks, *Water Resour. Res.*, 39, <https://doi.org/10.1029/2002WR001521>, 2003.

804 McGrath, H., Bourgon, J.-F., Proulx-Bourque, J.-S., Nastev, M., and Abo El Ezz, A.: A comparison of  
805 simplified conceptual models for rapid web-based flood inundation mapping, *Nat. Hazards*, 93, 905–920,  
806 <https://doi.org/10.1007/s11069-018-3331-y>, 2018.

807 Medeiros, S., Hagen, S., Weishampel, J., and Angelo, J.: Adjusting Lidar-Derived Digital Terrain Models in  
808 Coastal Marshes Based on Estimated Aboveground Biomass Density, *Remote Sens.*, 7, 3507–3525,  
809 <https://doi.org/10.3390/rs70403507>, 2015.

810 Morton, R. A. and Barras, J. A.: Hurricane Impacts on Coastal Wetlands: A Half-Century Record of Storm-  
811 Generated Features from Southern Louisiana, *J. Coast. Res.*, 27, 27–43,  
812 <https://doi.org/10.2112/JCOASTRES-D-10-00185.1>, 2011.

813 Muis, S., Lin, N., Verlaan, M., Winsemius, H. C., Ward, P. J., and Aerts, J. C. J. H.: Spatiotemporal patterns  
814 of extreme sea levels along the western North-Atlantic coasts, *Sci. Rep.*, 9, 3391,  
815 <https://doi.org/10.1038/s41598-019-40157-w>, 2019.

816 Muñoz, D. F., Cissell, J. R., and Moftakhari, H.: Adjusting Emergent Herbaceous Wetland Elevation with  
817 Object-Based Image Analysis, Random Forest and the 2016 NLCD, *Remote Sens.*, 11, 2346,  
818 <https://doi.org/10.3390/rs11202346>, 2019.

819 Muñoz, D. F., Moftakhari, H., and Moradkhani, H.: Compound effects of flood drivers and wetland  
820 elevation correction on coastal flood hazard assessment, *Water Resour. Res.*, 56, e2020WR027544,  
821 2020.

822 Muñoz, D. F., Muñoz, P., Moftakhari, H., and Moradkhani, H.: From local to regional compound flood  
823 mapping with deep learning and data fusion techniques, *Sci. Total Environ.*, 782, 146927, 2021.

824 Muñoz, D. F., Abbaszadeh, P., Moftakhari, H., and Moradkhani, H.: Accounting for uncertainties in  
825 compound flood hazard assessment: The value of data assimilation, *Coast. Eng.*, 171, 104057,  
826 <https://doi.org/10.1016/j.coastaleng.2021.104057>, 2022.

827 Nardi, F., Vivoni, E. R., and Grimaldi, S.: Investigating a floodplain scaling relation using a  
828 hydrogeomorphic delineation method, *Water Resour. Res.*, 42,  
829 <https://doi.org/10.1029/2005WR004155>, 2006.

830 Roelvink, J. A. and Banning, G. K. F. M. V.: Design and development of DELFT3D and application to  
831 coastal morphodynamics, *Oceanogr. Lit. Rev.*, 11, 925, 1995.

832 Rogers, J. N., Parrish, C. E., Ward, L. G., and Burdick, D. M.: Improving salt marsh digital elevation model  
833 accuracy with full-waveform lidar and nonparametric predictive modeling, *Estuar. Coast. Shelf Sci.*, 202,  
834 193–211, <https://doi.org/10.1016/j.ecss.2017.11.034>, 2018.

835 Samela, C., Manfreda, S., Paola, F. D., Giugni, M., Sole, A., and Fiorentino, M.: DEM-Based Approaches  
836 for the Delineation of Flood-Prone Areas in an Ungauged Basin in Africa, *J. Hydrol. Eng.*, 21, 06015010,  
837 [https://doi.org/10.1061/\(ASCE\)HE.1943-5584.0001272](https://doi.org/10.1061/(ASCE)HE.1943-5584.0001272), 2016.

838 Samela, C., Troy, T. J., and Manfreda, S.: Geomorphic classifiers for flood-prone areas delineation for  
839 data-scarce environments, *Adv. Water Resour.*, 102, 13–28,  
840 <https://doi.org/10.1016/j.advwatres.2017.01.007>, 2017.

841 Schieder, N. W., Walters, D. C., and Kirwan, M. L.: Massive Upland to Wetland Conversion Compensated  
842 for Historical Marsh Loss in Chesapeake Bay, USA, *Estuaries Coasts*, 41, 940–951,  
843 <https://doi.org/10.1007/s12237-017-0336-9>, 2018.

844 Sullivan, J. C., Torres, R., and Garrett, A.: Intertidal Creeks and Overmarsh Circulation in a Small Salt  
845 Marsh Basin, *J. Geophys. Res. Earth Surf.*, 124, 447–463, <https://doi.org/10.1029/2018JF004861>, 2019.

846 Teng, J., Vaze, J., Dutta, D., and Marvanek, S.: Rapid Inundation Modelling in Large Floodplains Using  
847 LiDAR DEM, *Water Resour. Manag.*, 29, 2619–2636, <https://doi.org/10.1007/s11269-015-0960-8>, 2015.

848 Thomas, A., Dietrich, J., Asher, T., Bell, M., Blanton, B., Copeland, J., Cox, A., Dawson, C., Fleming, J., and  
849 Luettich, R.: Influence of storm timing and forward speed on tides and storm surge during Hurricane  
850 Matthew, *Ocean Model.*, 137, 1–19, <https://doi.org/10.1016/j.ocemod.2019.03.004>, 2019.

851 U.S. Army Corps of Engineers: Current Channel Condition Survey Reports and Charts. Savannah Harbor.,  
852 2017.

853 Wamsley, T. V., Cialone, M. A., Smith, J. M., Atkinson, J. H., and Rosati, J. D.: The potential of wetlands in  
854 reducing storm surge, *Ocean Eng.*, 37, 59–68, <https://doi.org/10.1016/j.oceaneng.2009.07.018>, 2010.

855 Williams, W. A., Jensen, M. E., Winne, J. C., and Redmond, R. L.: An Automated Technique for  
856 Delineating and Characterizing Valley-Bottom Settings, in: *Monitoring Ecological Condition in the*  
857 *Western United States: Proceedings of the Fourth Symposium on the Environmental Monitoring and*  
858 *Assessment Program (EMAP), San Francisco, CA, April 6–8, 1999*, edited by: Sandhu, S. S., Melzian, B. D.,  
859 Long, E. R., Whitford, W. G., and Walton, B. T., Springer Netherlands, Dordrecht, 105–114,  
860 [https://doi.org/10.1007/978-94-011-4343-1\\_10](https://doi.org/10.1007/978-94-011-4343-1_10), 2000.

861 Wing, O. E. J., Sampson, C. C., Bates, P. D., Quinn, N., Smith, A. M., and Neal, J. C.: A flood inundation  
862 forecast of Hurricane Harvey using a continental-scale 2D hydrodynamic model, *J. Hydrol. X*, 4, 100039,  
863 <https://doi.org/10.1016/j.hydroa.2019.100039>, 2019.

864 Wu, W., Zhou, Y., and Tian, B.: Coastal wetlands facing climate change and anthropogenic activities: A  
865 remote sensing analysis and modelling application, *Ocean Coast. Manag.*, 138, 1–10,  
866 <https://doi.org/10.1016/j.ocecoaman.2017.01.005>, 2017.

867 Yan, H. and Moradkhani, H.: A regional Bayesian hierarchical model for flood frequency analysis, *Stoch.*  
868 *Environ. Res. Risk Assess.*, 29, 1019–1036, 2015.

869 Zheng, X., Maidment, D. R., Tarboton, D. G., Liu, Y. Y., and Passalacqua, P.: GeoFlood: Large-Scale Flood  
870 Inundation Mapping Based on High-Resolution Terrain Analysis, *Water Resour. Res.*, 54, 10,013–10,033,  
871 <https://doi.org/10.1029/2018WR023457>, 2018a.

872 Zheng, X., Tarboton, D. G., Maidment, D. R., Liu, Y. Y., and Passalacqua, P.: River Channel Geometry and  
873 Rating Curve Estimation Using Height above the Nearest Drainage, *JAWRA J. Am. Water Resour. Assoc.*,  
874 54, 785–806, <https://doi.org/10.1111/1752-1688.12661>, 2018b.

875

